Title: Effect of graphene material structure and iron oxides deposition method on morphology and properties of graphene/iron oxide hybrids

Author: Aleksandra Kordyka, Jerzy Kubacki, Yevgen Mamunya, Sławomira Pusz, Ivanka Stoycheva, Urszula Szeluga [i in.]

Citation style: Kordyka Aleksandra, Kubacki Jerzy, Mamunya Yevgen, Pusz Sławomira, Stoycheva Ivanka, Szeluga Urszula [i in.] (2022). Effect of graphene material structure and iron oxides deposition method on morphology and properties of graphene/iron oxide hybrids. "Applied Surface Science" (2022), Vol. 573, art. no. 151567, s. 1-14. DOI: 10.1016/j.apsusc.2021.151567

Applied Surface Science 573 (2022) 151567

Contents lists available at ScienceDirect

Applied Surface Science

journal homepage: www.elsevier.com/locate/apsusc

Full Length Article

Effect of graphene material structure and iron oxides deposition method on morphology and properties of graphene/iron oxide hybrids

Anastasiia Kobyliukh [a], Karolina Olszowska [a], Marcin Godzierz [a], Aleksandra Kordyka [a], Jerzy Kubacki [b,c], Yevgen Mamunya [d], Sławomira Pusz [a], Ivanka Stoycheva [e], Urszula Szeluga [a,*]

[a] Centre of Polymer and Carbon Materials, Polish Academy of Sciences, Zabrze, M. Curie-Skłodowskiej 34, Zabrze 41-819, Poland
[b] A. Chełkowski Institute of Physics, University of Silesia, Uniwersytecka 4, Katowice, Poland
[c] Silesian Center for Education and Interdisciplinary Research, 75 Pulku Piechoty 1A, Chorzow, Poland
[d] Institute of Macromolecular Chemistry NAS of Ukraine, 48, Kharkovskoe shosse, Kiev 02160, Ukraine
[e] Institute of Organic Chemistry with Centre of Phytochemistry, Bulgarian Academy of Sciences, Acad. G. Bonchev str, BL. 9, 1113 Sofia, Bulgaria

ARTICLE INFO

Keywords:
Iron oxide nanoparticles
Maghemite
Magnetite
Graphene materials
Graphene/iron oxide hybrids

ABSTRACT

In this work, various facile approaches were applied to prepare hybrids of graphene nanoplatelets (GNPs) and graphene oxide (GO) with iron oxides (IO) nanoparticles (NPs). The IO NPs were synthesized and deposited on the graphene surfaces via: (1) co-precipitation using Fe (II) and Fe (III) salts, (2) homogeneous precipitation of Fe_2O_3 from $FeCl_3$ solution, (3) the attaching of Fe_2O_3 NPs functionalized with 3-aminopropyltrimethoxysilane to graphene surfaces of GO and GNPs. The effects of the graphene material and preparation procedure on the structural characteristics of the hybrids were studied. Their morphology was studied by scanning electron microscopy and transmission microscopy. Lattice parameters and crystallite sizes of the synthesized hybrid materials were assessed by X-ray diffraction. Raman spectroscopy was used to determine the change of order degree of graphene structures as a results of IO NPs deposition and interactions IO NPs with graphene sheets. Binding energy for IO NPs and graphene structures were determined by photoelectron X-ray spectroscopy. Thermogravimetric analysis was applied to find differences in the thermal stability of hybrids. The hybrids are proposed as nanofillers to polymer composites, however they have large potential applications as supercapacitors, advanced anode materials for lithium-ion batteries, magnetically targeted drug delivery, and magnetic resonance imaging.

1. Introduction

In recent years, a lot of studies on the preparation and application of various structures containing graphene layers have been undertaken and received great attention. Graphene materials due to their indisputable advantages, i.e. high mechanical strength of the C—C bonds of their hexagonal lattice, high thermal stability, and electrical and thermal conductivities [1,2], are one of the most promising future-oriented materials. The honeycomb carbon layers, as basic structural units of graphene materials, can be variously arranged and characterized by different aspect ratios, type and number of functional groups attached to the graphene layers, and the ratio of sp^2 to sp^3 carbon atoms [2,3]. The most widely used graphene-based structures are graphene oxide (GO), reduced graphene oxide (rGO) and carbon nanotubes (CNTs). They are largely studied in terms of their application, primarily in the construction of electronic and electrochemical devices, the immobilization of a large number of materials including cells, drugs, biomolecules, metals, and functioning molecules, and as fillers of polymer systems increasing the possibility of obtaining new polymer composites [4,5].

However, the strong tendency to agglomeration of graphene layers resulting from their noticeable lateral area to thickness ratio, as well as strong surface interactions, hinders many applications. These disadvantageous features justify the need of hybridization or functionalization of graphene surfaces to obtain new hybrid materials with better properties [4,5]. Nowadays, the new approaches to produce hybrid materials based on different graphene structures and iron oxide (IO) nanoparticles (NPs) with strongly reduced tendency to agglomeration and improved magnetic properties is increasingly focused [6,7]. Graphene/IO hybrids can be designed based on the combination of IO NPs with CNTs [8-11], graphene nanosheets (GNPs) [12], GO [13], or rGO [14,15].

The graphene/IO nanohybrids can be obtained using one-step IO NPs

* Corresponding author.
E-mail address: uszeluga@cmpw-pan.edu.pl (U. Szeluga).

https://doi.org/10.1016/j.apsusc.2021.151567
Received 24 June 2021; Received in revised form 29 September 2021; Accepted 8 October 2021
Available online 9 October 2021

preparation methods in the presence of GO or GNPs, e.g. solution precipitation including co-precipitation and homo-precipitation [16-18]. They can also be prepared using IO NPs previously synthesized by thermal decomposition [16], sol–gel [16,18,19], hydrothermal/solvothermal [16,18,20,21], microemulsion [16], microwave-assisted [22], sonochemical decomposition, gas phase deposition, electrospinning [23], electrodeposition, and pulsed laser ablation [24] methods, etc, and then deposited on the GO or rGO surface. Various morphologies (spherical, cubic, disk, flower-shaped, elongated), size, surface characteristics and physicochemical properties of IO NPs are responsible for different structural and magnetic properties of graphene/IO hybrids, and the selection of the most preferable synthesis route is crucial to obtain desirable products. The improvement of the IO NPs grafting efficiency with oxygen groups of graphene materials can be achieved by the functionalization of IO NPs with reactive agents, e.g. 3-aminopropyltrimethoxysilane (APTES) [25], amine [26], etc.

Mederos-Henry et al. [7] studied the effect of preparation route on the composition and quality of the IO products. They compared three different methods of deposition of magnetite NPs on the surface of GO or CNTs, i.e., direct co-precipitation, covalent linkage and the solvothermal procedure. According to the authors, the co-precipitation method was not the most preferred method for obtaining pure mono-component IO phase on the carbon materials due to the presence of two different iron ions. The authors indicated the polyol solvothermal method as the most advantageous for preparing graphene/IO hybrids, because of no difficulties in controlling the process, which in turn led to obtaining stable electromagnetic properties. Albert et al. [13] verified the effect of the ratio between IO and GO on hybrid structures obtained in co-precipitation and emulsion procedures. The smallest size of IO NPs on the graphene layers, decisive to achieve hybrid materials with the best magnetic properties, was observed for the highest IO loading. Askari et al. [27] synthesized a GO/Fe_3O_4 hybrid by traditional co-precipitation of a mixture of $Fe^{2+}$and Fe^{3+} ions with reduced tendency of graphene structures to agglomeration, and without surfactants for nanoparticles stabilization in the base fluid. Chandra et al. [28] obtained superparamagnetic rGO/Fe_3O_4 hybrids by the hydrazine reduction of GO/Fe_3O_4 precursor, which was prepared by precipitation of a mixture of Fe^{2+} and Fe^{3+}ions. Other reduction routes of GO/IO hybrids by facile green methods using plant extracts are recognized because of their low cost, efficiency, and eco-friendliness. The synthesis of iron and IO NPs deposited on rGO surfaces using green, oolong and black teas, as well as eucalyptus leaf extract, protein, vitamins or polyphenols have been proposed [29,30]. rGO/Fe_2O_3 hybrids were synthesized using a supercritical CO_2 thermal reduction of $Fe(NO_3)_3{\cdot}9H_2O$ and GO dispersion [31]. Finally, rGO/Fe_2O_3 hybrids were prepared in other than powder form, i.e., as aligned paper in vertical or horizontal directions obtained using filtration in a controlled magnetic field. Rosaiah et al. [32] studied magnetic GO hybrids obtained by a facile and cost-effective graphenothermal synthesis based on the simultaneous reduction of GO to 3D rGO, and micro-sized Fe_2O_3 particles to Fe_3O_4 NPs, under argon environment in the temperature range of 600–700 °C. Palakollu et al. [32] proposed the hybrid obtained by deposition of Fe_2O_3 NPs on the rGO layers as a component of glassy carbon electrodes for electrochemical detecting of acetaminophen in clinical application.

In recent years, besides extended innovative works on graphene/IO hybrids and their promising properties, comprehensive research has been started on more complex hybrid materials. These developments were performed primarily to enhance key performance parameters and expand the possibilities of their use in relation to graphene/IO hybrids. Complex materials, in addition to iron oxides and graphene or carbon nanotubes, also contain other additional components, i.e. hybrid oxides [33], nitrogen-doped materials [34], functionalized graphene materials [35], graphene foams [36], or polymers [37]. The most intensive studies on the three dimensional graphene/CNTs/IO structures have been performed [38–40] because of their potential applications as anode material for lithium-ion batteries, supercapacitors, catalysts, systems to removal pollution from water, electrochemical sensors, etc.

In this paper, the effect of the structure of graphene support material and the procedure of IO NPs deposition on graphene layers on structural parameters, morphology, and thermal properties of graphene/IO hybrids is discussed. GO with high content of oxygen functional groups synthesized by an improved Hummers method, and graphene nanoplatelets (GNPs) as a highly reduced graphene form, are used as carbon supports of iron compounds. The IO NPs were synthesized and deposited on the graphene surfaces by one-step direct co-precipitation and homo-precipitation routes. The third method consisted of two steps: in the first step Fe_2O_3 NPs were functionalized with3-aminopropyltrimethoxysilane (APTES) and then they were attached to graphene surfaces of GO and GNPs. Additionally, the co-precipitation procedure under inert atmosphere (nitrogen) was performed only for GNPs as graphene support to obtain a hybrid with embedded Fe_3O_4 NPs. The structural parameters of the obtained hybrids, determined using microscopic techniques (SEM/EDX, TEM), X-ray diffraction (XRD) and spectroscopic methods (Raman, XPS), are analyzed and discussed.

These hybrid materials are proposed as nanofillers for polymer composites, however they have large potential applications in electronics such as supercapacitors, advanced anode materials for lithium-ion batteries, and in medicine.

2. Experimental

2.1. Materials and reagents

Graphite powder (<50 μm, carbon ≥ 99,5 %, true density 2,2 g/cm^3), GNPs (xGNP M−15, oxygen < 1%, average lateral dimension 15 μm, average thickness 6–8 nm, specific surface area 120–150 m^2/g, bulk density 0.03–0.1 g/cm^3), superparamagnetic iron (II) oxide nanoparticles (SPION, Fe_2O_3, average dimensions < 50 nm), and APTES, hydrazine hydrochloride ($N_2H_4{\cdot}2HCl$) were purchased from Sigma Aldrich. Iron (II) chloride tetrahydrate ($FeCl_2{\cdot}4H_2O$), iron (III) chloride hexahydrate ($FeCl_3{\cdot}6H_2O$) sodium chloride (NaCl), sulphuric acid (H_2SO_4, 95%), o-phosphoric acid (H_3PO_4, 85%), manganese permanganate ($KMnO_4$), hydrogen peroxide (H_2O_2, 30%), ammonia water ($NH_3{\cdot}H_2O$), sodium hydroxide (NaOH), urea ($CO(NH_2)_2$), dimethyloformamid (DMF), and ethanol (96%) were purchased from Avantor Performance Materials Poland S.A.

2.2. Preparation methods

2.2.1. Synthesis of GO

Graphene oxide was synthesized using the modified Hummers method by oxidation of graphite powder in a process consisting of several stages, described in detail by Kumanek et al. [40].

2.2.2. Synthesis of GO/IO_{cp} and GNP/IO_{cp} hybrids by co-precipitation

GO or GNPs were dispersed by ultrasonication in 100 mL of deionized water (DI) for 30 min. 0.1 g of $FeCl_2{\cdot}4H_2O$ was diluted in 50 mL of DI and 0.2 g of $FeCl_3{\cdot}6H_2O$ was diluted in 100 mL of DI separately. These solutions were added dropwise to graphene material dispersion while stirring for 30 min. To reach the pH of 11–12, a small amount of $NH_3{\cdot}H_2O$ (10 mL) was added to this mixture. After that the solution was heated to 50 °C for 30 min while stirring. Then the solution was filtered, washed a few times with DI and ethanol and dried at 80 °C for 24 h.

The co-precipitation procedure was also performed for GNPs under a nitrogen atmosphere; however, some conditions were modified. GNPs were dispersed in a round three-neck flask in 100 mL DI by ultrasonic treatment for 30 min. The nitrogen was purged through the GNPs dispersion until it filled the flask space. Then 0.01 mol $FeCl_2{\cdot}4H_2O$ and 0.02 mol $FeCl_3{\cdot}6H_2O$, dissolved separately in 100 mL DI, were added using droppers placed in the necks of the flask. After that, 8 mol of NaOH dissolved in 100 mL DI was added to the reaction mixture and stirring was continued for 3 h. Then the solution was filtered, washed a few

times with DI and ethanol, and dried at 80 °C for 24 h.

2.2.3. Synthesis of GO/IO$_{hp}$ and GNP/IO$_{hp}$ hybrids by homo-precipitation

To prepare GO and GNP hybrids decorated with Fe_2O_3, 0.81 g (5 mmol) of $FeCl_3$ was dissolved in 50 mL of DI and 9.0 g (150 mmol) of CO $(NH_2)_2$ in 50 mL of DI separately. 0.1 g of GO or GNPs and 50 mL of water solutions of iron (III) chloride and urea solution was added to the mixture drop by drop while stirring. Then the solution was ultrasonicated in an ultrasonic bath for 30 min and heated to 90 °C for 1.5 h. After cooling down to room temperature, to the continuously stirred mixture, 0.5 mL of 64–65% hydrazine solution was added and further stirred. Then the mixture was filtered, washed with deionized water and ethanol several times and dried at 80 °C for 24 h.

2.2.4. Synthesis of APTES functionalized Fe_2O_3 (IO$_{APTES}$) and GO/IO$_{APTES}$ and GNP/IO$_{APTES}$ hybrids

0.1 g of SPION (Fe_2O_3 NPs) and 2 g of APTES dissolved in 100 g of anhydrous ethanol were used. Next, 20 mL of deionized water was added, and the solution was stirred using a mechanical stirrer at 78 °C for 4 h. Then the solution contained IO$_{APTES}$ NPs was filtered and washed several times with deionized water and ethanol and dried in the oven at 60 °C for 24 h. At the same time, 0.2 g of GO or GNPs was dispersed in 100 mL of DMF by ultrasonic probe for 30 min and then 0.5 g of IO$_{APTES}$ NPs was added to the dispersion and ultrasonicated for 30 min. In the next steps the solution was stirred at 105 °C for 5 h, then filtered and washed several times with deionized water and ethanol, and then dried in an oven at 60 °C for 24 h.

2.3. Characterization methods

Scanning electron microscopy investigations were carried out with the SEM FEI Quanta 250 FEG equipped with a secondary electron detector (EDT), in high vacuum mode, with accelerating voltages of 10.0–20.0 kV. The samples were fixed on a measuring holder using carbon tape. The quantitative elemental analyses of the surfaces of the hybrid materials was carried out using SEM technique coupled with the energy-dispersive X-ray spectroscopy (EDX).

The TEM studies were performed using Tecnai G2 F20 microscope (FEI Company) equipped with a field emission gun, operated at the acceleration voltage of 200 kV. TEM images were recorded on the Gatan Rio 16 CMOS camera (Gatan) and processed with Digital Micrograph software (Gatan). The samples for the TEM studies were dispersed in ethanol by ultrasonic treatment. The suspension was then placed on a cooper grid 200 mesh (Quantifoil), and after evaporation of alcohol, the specimens were inserted into the microscope chamber and analyzed.

XRD measurements were performed using D8 Advance diffractometer (Bruker) with Cu-Kα cathode ($\lambda = 1.54$ Å). The scan rate was 0.6°/min with scanning step 0.02° in the range of 5° to 90° 2Θ, using Bragg-Brentano geometry. The fitted phases were identified using the DIFFRAC.EVA program with ICDD PDF#2 database. Lattice parameters, crystal size and lattice strain were calculated using Rietveld refinement in the TOPAS 6 program, based on the Williamson-Hall theory [41-43]. The pseudo-Voigt function was used in the description of diffraction line profiles at the Rietveld refinement. The R_{wp} (weighted-pattern factor) and S (goodness-of-fit) parameters were used as numerical criteria of the quality of the fit of calculated to experimental diffraction data.

The structural order of graphene precursors and their IO hybrids was determined by Raman spectroscopy. Raman spectra were recorded on Witec Alfa M300 + spectrometer with a Nd-YAG laser beam operated with an excitation wavelength of 532 nm and a laser power of 50 mW. The measurement parameters were as follows: laser power – 1 mW, time of exposure – 3 s, number of accumulations – 100, and an acquisition range of 0–3800 cm^{-1}. For each sample, approximately 10 points were analyzed to obtain insight into the sample structural homogeneity by using the spectrometer live mode without recording the spectra. The ratios of the intensity of the D and G peaks (I_D/I_G) and their areas (A_D/A_G), estimating the ordering of the graphene sheets, were determined using Witec Project 4.1 software.

The X-ray photoelectron spectroscopy (XPS) measurements using an Al-K$_\alpha$ ($h\nu = 1486.6$ eV) monochromatized X-ray source were performed on a multifunctional electron spectrometer PHI5700/660 Physical Electronics. For each sample, the photoelectron spectrum in a wide range of binding energies from –2 eV to 1400 eV with precise measurements of the spectral lines of individual components of the surface layer and valence band measurements were determined. The average free path of photoelectrons was determined as approx. 5 Å – 40 Å for the excitation energy used, i.e., the information about the chemical composition obtained from the spectra concerns the surface layer of such a thickness. The scale of the energy was calibrated to the positions of the Au 4f7/2, Ag 3d5/2 and Cu2p3/2 peaks, and the energy resolution was 0.3 eV. The following routines were applied: the Shirley method for background subtraction and a standard method for deconvolution using a mixed Gaussian-Lorentzian line shape. The chemical composition was determined by integrating the appropriate photoemission lines using the MULTIPAK program from Physical Electronics.

Thermogravimetric analysis (TGA) was performed with a TGA/DSC1 Mettler-Toledo thermal analyzer with a heating rate of 10 °C/min in a stream of nitrogen (60 mL/min).

3. Results and discussion

During the synthesis of graphene hybrids with deposited IO NPs, positively charged iron (III) ions are adsorbed and anchored on negatively charged oxygen functional groups, found in significant numbers in GO and in much less numbers on the surface of GNPs, but also on structural defects of graphene sheets. Fe^{3+} ions begin to hydrolyze, nucleate, and crystallize as Fe_2O_3 crystals form to produce the desired graphene-based hybrids. The iron (II) ions in the presence of iron (III) ions in the co-precipitation route under nitrogen contributed to the formation of the Fe_3O_4 crystal phase. Hydrazine used in the homo-precipitation procedure can be a reduction agent towards both iron ions and GO, affecting the reduction of the oxygen groups. The same may be the case of DMF used in the procedure of grafting IO$_{APTES}$ NPs on the graphene sheets. Therefore, it is very important to understand the effect of the synthesis conditions and the precursor structure on the characterization of IO crystals deposited on the graphene support that will provide valuable information regarding the control of the hybrid's morphology.

3.1. Structural parameters and morphology of hybrids from SEM, TEM and XRD methods

The SEM images of GO and GNPs precursors as well as GO/IO and GNP/IO hybrid materials are shown in Fig. 1. GO exhibits a typical layered structure with smooth surface and wrinkled edges (Fig. 1a). According to Fig. 1b–d, GO was coated by IO NPs in varying degrees depending on the procedure, simultaneously keeping the sheet-like structure. The surface of the hybrid material obtained by the attaching of IO NPs functionalized with APTES to the GO sheets was covered in the slightest degree by IO NPs, mainly at the edges of graphene sheets. IO NPs obtained by the homo-precipitation procedure were densely and evenly attached on the GO surface (Fig. 1 c), forming a sheet-like structure hybrid. The aggregation of IO NPs unevenly formed in the GO sheets is evident for the hybrid obtained by co-precipitation (Fig. 1b). Similar morphological observations were noted for GNP-based hybrids. The highest degree of IO NPs agglomeration on the graphene layers was observed for GNP/IO$_{cp}$ hybrid (Fig. 1f). The above structural specifics were further confirmed by TEM observations. The elemental composition of the GO/IO and GNP/IO hybrid specimens was performed using EDX spectroscopy.

The relative atomic concentrations of C, O and Fe elements for the various samples are listed in Table 1. The carbon/oxygen (C/O) atomic

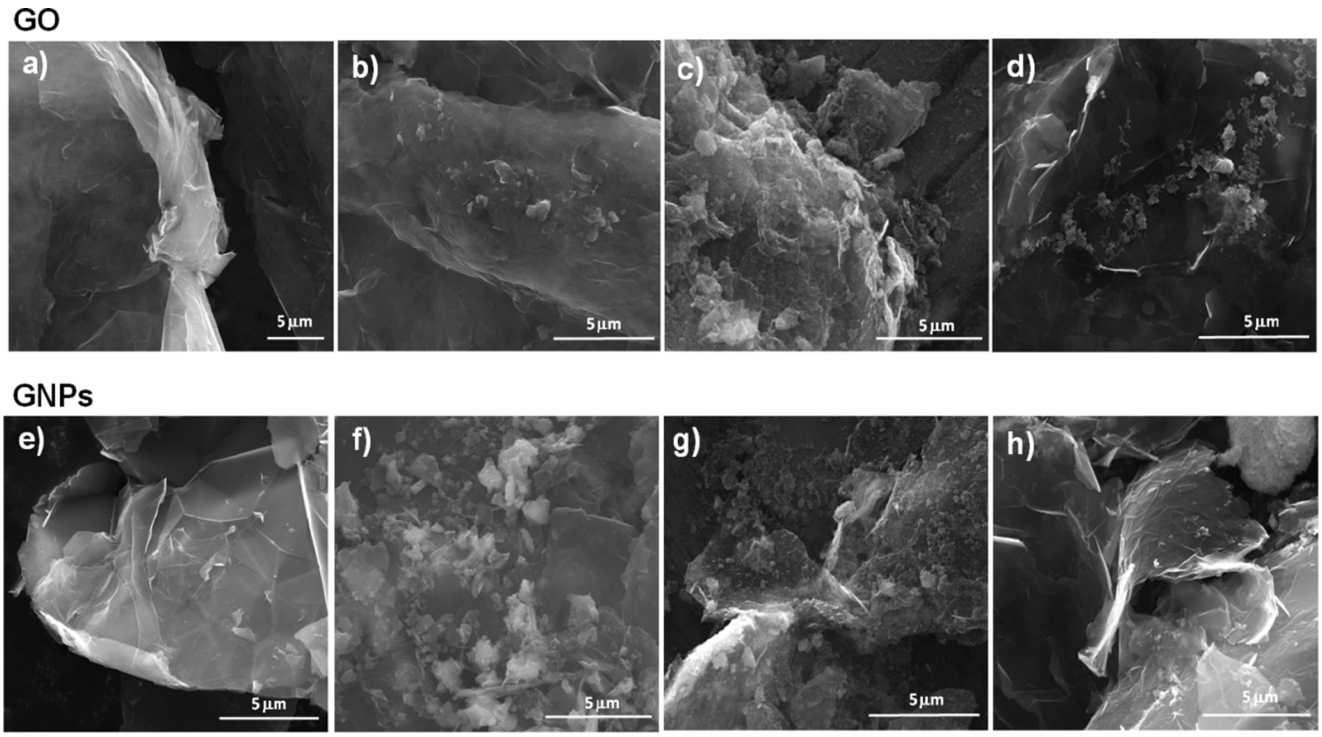

Fig. 1. SEM images of a) GO sheets, b) GO/IO_{cp}, c) GO/IO_{hp}, d) GO/IO_{APTES}, e) GNP sheets, f) GNP/IO_{cp}, g) GNP/IO_{hp}, h) GNP/IO_{APTES}.

Table 1
Atomic concentration and C/O ratio for GO- and GNP-based hybrids by EDX method.

	C [at.%]	O [at.%]	Fe [at.%]	C/O
GO	76.2	23.4	–	3.26
GO/IO_{cp}	64.3	23.3	12.4	2.76
GO/IO_{hp}	41.9	31.8	23.9	1.32
GO/IO_{APTES}	68.8	21.9	8.9	3.14
GNPs	95.5	4.1	–	23.3
GNP/IO_{cp}	81.2	9.3	9.2	8.7
GNP/IO_{hp}	69.2	15.9	13.9	4.35
GNP/IO_{APTES}	90.9	6.2	2.6	14.7

ratio indicates the degree of graphene surface occupation by deposited IO NPs, and additionally assesses the nature of oxygen functionalities. The GO exhibited the C/O atomic ratio of 3.26, consistent with the range reported for oxidized graphene material [3,44]. The C/O ratio decreased for all GO-based hybrids as compared to the GO precursor. This is evidence of a higher oxygen concentration as a result of introduction of IO NPs despite the replacement and elimination of some oxygen functional groups on the GO sheets.

In the case of GNP-based hybrid samples, a similar trend of the C/O ratio was observed, but the absolute C/O ratio values were significantly higher than that for GO-based analogous materials. The highest atomic content of Fe was recorded for GO/IO_{hp} and GNP/IO_{hp} hybrids, while the lowest concentration of Fe was found for hybrids obtained by grafting of IO_{APTES} NPs to the graphene layers of both GO and GNPs. It should be noted that the contents of IO NPs deposited on the graphene oxide surface are larger than on their GNP-based counterparts. This is obviously related to the content of oxygen groups.

Fig. 2a and e show the TEM images of GO and GNPs support materials. The typical wrinkles or wavy features are seen for both GO and GNPs, and these observations are in accordance with the SEM images. All hybrid materials, independently of the graphene precursor and preparation method, maintained a two-dimensional sheet morphology. After the deposition reaction no IO NPs were found outside of the graphene sheets of GO because of the strong interfacial interactions between graphene sheets and IO NPs.

A similar phenomenon was observed for IO NPs deposited onto GNPs with significantly lower content of oxygen species. Considering the homogeneity and density of IO NPs distribution on the graphene sheets, it was rational to speculate that the most suitable hybrid material could be obtained via homo-precipitation. It was also observed that IO NPs exhibited the shapes like flat bars, both on the GO surface (Fig. 2c) and on the carbon sheets of GNPs (Fig. 2g). The TEM images of hybrids produced by co-precipitation show undefined shaped IO NPs forming agglomerates on graphene sheets (Fig. 2b and f) [45]. These large agglomerates can be the effect of uncontrolled nucleation caused by the water present in the reaction medium and responsible for increasing rates of hydrolysis and condensation of both Fe^{3+} and Fe^{2+} ions [45]. The structure and other parameters for GNP-based hybrid obtained by co-precipitation under nitrogen are discussed separately in the last Section 3.5.

A definitely different structure is observed for GO/IO_{APTES} and GNP/IO_{APTES} hybrids, in which IO NPs are anchored substantially at and near the graphene edges (Fig. 2d and h). Generally, the crystals of IO NPs functionalized with APTES have an irregular hexagonal form, however amorphous NPs also exist.

The crystalline structure of GO, GNP and their hybrids with IO NPs were characterized by X-ray diffraction. As shown in Fig. 3a for GO and GO/IO hybrids, the peaks at 2θ values of around 26° and 43° are assigned to diffraction of the (002) and (004) carbon planes in GO structure, respectively [14], whereas the broad (001) diffraction peak at approx. 12.5° is attributed to the characteristic diffraction peak of GO sheets with d-spacing of 3.355 Å [25,46]. For GNPs, the intense peak occurs at about 26.5° (with d-spacing of 3.36 Å), which is typical for (002) plane of graphitic structure. Calculated lattice parameters of both GO and GNP structures are in good agreement with ICDD data (Tab. 2.), however, in the case of their hybrids, larger lattice strains were found in GO-based samples, probably because of the oxide groups attached to graphene layers.

Crystalline phases of iron compounds found in hybrids were the following: the cubic γ-Fe_2O_3 (Maghemite, PDF#00–039-1346) and three

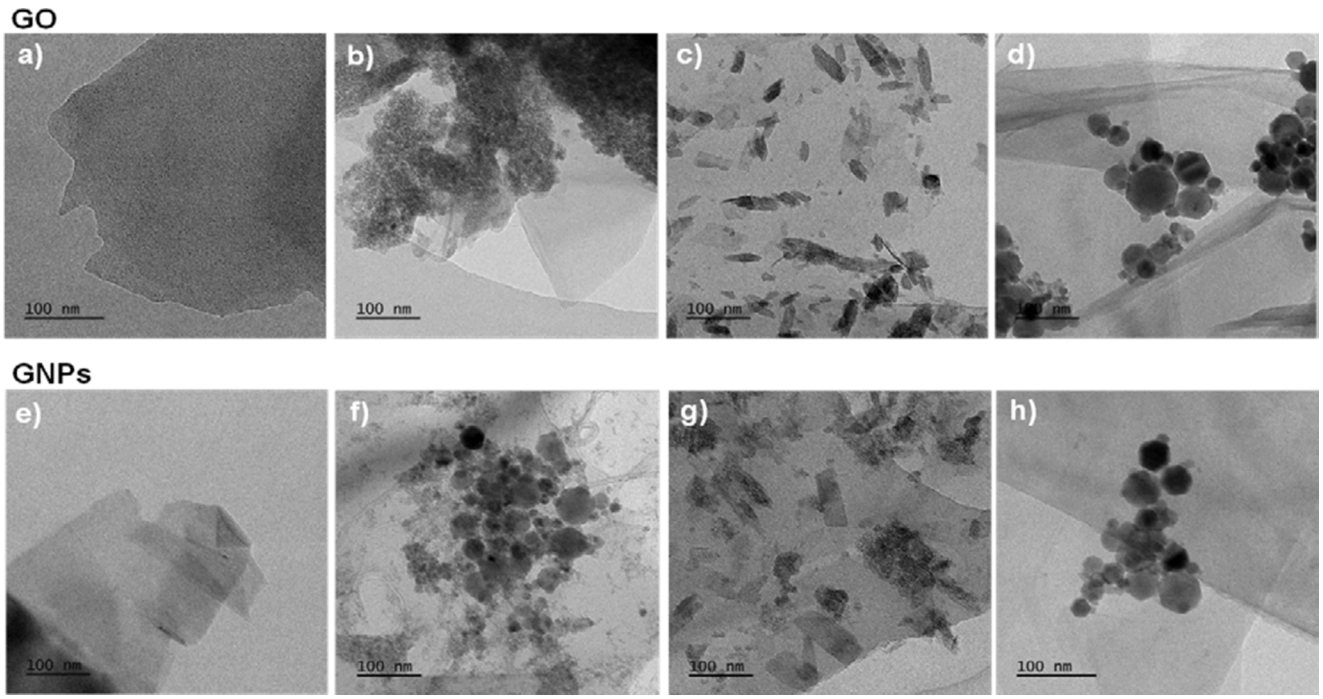

Fig. 2. TEM images of a) GO sheets, b) GO/IO_{cp}, c) GO/IO_{hp}, d) GO/IO_{APTES}, e) GNP sheets, f) GNP/IO_{cp}, g) GNP/IO_{hp}, h) GNP/IO_{APTES}.

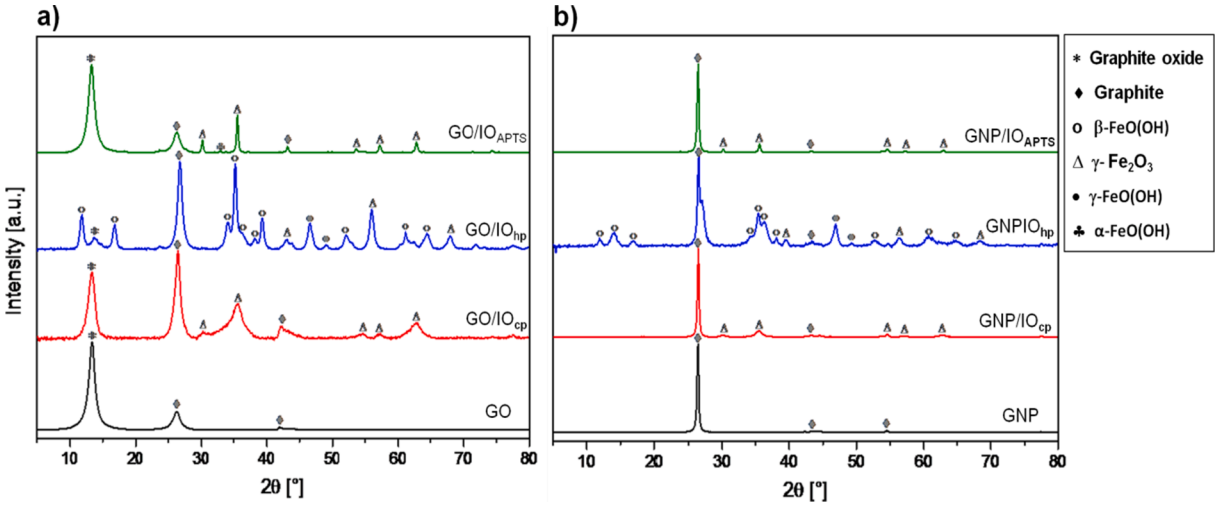

Fig. 3. X-Ray diffraction patterns of (a) GO-based and (b) GNP-based hybrids.

forms of FeO(OH) (anhydrous ferric oxyhydroxide): orthorhombic α-FeO(OH) (Goethite, PDF#01–076-7164), tetragonal β-FeO(OH) (Akaganeite, PDF#00–034-1266) and orthorhombic γ-FeO(OH) (Lepidocrocite, PDF#00–044-1415). Based on the XRD patterns, the presence of maghemite, identified as the primary product of crystallization of amorphous Fe_2O_3 [47], was confirmed for all hybrids, independently of applied GO or GNP precursor and the method of preparation. In hybrids synthesized by homo-precipitation, in addition to maghemite, lepidocrocite and akaganeite were also found.

The peaks observed in GO/IO and GNP/IO XRD patterns at approx. 34-35°, 41°, 55° and 64° 2θ can be assign to the maghemite phase. These peaks are sharper and more intense for GO-based hybrids, due to the larger crystallite size of maghemite deposited on the GO surfaces in comparison to GNPs [48,49].

Depending on the method of preparation of GO/IO and GNPs/IO hybrids, different kinds of Fe compounds crystalline phases, as well as the size of their particles, were obtained (Table 2).

Using the co-precipitation method and deposition of IO NPs functionalized with APTES on the graphene surfaces, it is possible to obtain very small crystallites (approx. 10 nm and 40 nm, respectively) of γ-Fe_2O_3, without any contribution of stress. For hybrids obtained by grafting of IO_{APTES} NPs, for GNP-based hybrid only γ- Fe_2O_3 crystallites were detected, while for GO-based hybrids, in addition to maghemite, α-FeO (OH) phase was also found. The homo-precipitation procedure for GO-based hybrid induced growth of γ- Fe_2O_3 crystallites up to approx. 80 nm, but also provoked a high lattice strain of the particles (above 0.5%). In the case of GNP-based hybrid, the γ- Fe_2O_3 crystallites ~ 100 nm with almost 1.2% lattice strain were found. The co-precipitation method allowed to obtain one-phase IONPs such as maghemite deposited on the GO and GNPs, while the presence of fine crystallites of γ-FeO (OH) and highly strained crystallites of β-FeO(OH) with mean size approx. 20–25 nm were detected when GO- and GNP-based hybrids were prepared by the homo-precipitation method.

Summarizing, XRD results confirmed the presence of one-phase iron

Table 2
Lattice parameters of identified phases in GO/IO and GNP/IO hybrids.

Sample	Method	Phase	Space group	Lattice parameters ICDD [Å]	Lattice parameters, calculated [Å]	Crystallite size [nm]	Lattice strain [%]
GO	Base	Graphite	$P6_3/mmc$	a = 2.46 c = 6.71	a = 2.48 c = 6.76	13	0
		Graphite oxide	$P6_3/mmc$	–	–	22	0.01
GNPs	Base	Graphite	$P6_3/mmc$	a = 2.46 c = 6.71	a = 2.46 c = 6.72	49	0
GO/IO$_{cp}$	Co-precipitation	Graphite	$P6_3/mmc$	a = 2.46 c = 6.71	a = 2.48 c = 6.79	12	1.50
		γ-Fe_2O_3	$P4_132$	a = 8.35	a = 8.414	14	0.004
GNP/IO$_{cp}$	Co-precipitation	Graphite	$P6_3/mmc$	a = 2.46 c = 6.71	a = 2.46 c = 6.60	45	0
		γ-Fe_2O_3	$P4_132$	a = 8.35	a = 8.37	8	0
GO/IO$_{hp}$	Homo-precipitation	Graphite	$P6_3/mmc$	a = 2.46 c = 6.71	a = 2.45 c = 6.66	16	2.76
		γ-Fe_2O_3	$P4_132$	a = 8.35	a = 8.40	102	1.17
		β-FeO(OH)	I4/m	a = 10.54 c = 3.03	a = 10.52 c = 3.03	20	0.6
		γ-FeO(OH)	Bbmm	a = 12.52 b = 3.87 c = 3.07	a = 12.71 b = 3.91 c = 3.05	10	0
GNP/IO$_{hp}$	Homo-precipitation	Graphite	$P6_3/mmc$	a = 2.46 c = 6.71	a = 2.46 c = 6.71	50	0.33
		γ-Fe_2O_3	$P4_132$	a = 8.35	a = 8.39	83	0.596
		β-FeO(OH)	I4/m	a = 10.54 c = 3.03	a = 10.51 c = 2.98	29	0.63
		γ-FeO(OH)	Bbmm	a = 12.52 b = 3.87 c = 3.07	a = 12.52 b = 3.84 c = 3.06	8	0
GO/IO$_{APTES}$	Deposition of Fe_2O_3/ APTES	Graphite	$P6_3/mmc$	a = 2.46 c = 6.71	a = 2.46 c = 6.79	20	3.41
		γ-Fe_2O_3	$P4_132$	a = 8.35	a = 8.35	36	0
		α-FeO(OH)	Pnma	a = 9.95 b = 3.03 c = 4.61	a = 10.07 b = 2.99 c = 4.63	46	0.21
GNP/ IO$_{APTES}$	Deposition of Fe_2O_3/ APTES	Graphite	$P6_3/mmc$	a = 2.46 c = 6.71	a = 2.46 c = 6.71	49	0.12
		γ-Fe_2O_3	$P4_132$	a = 8.35	a = 8.34	43	0.13

(III) oxide nanoparticles deposited on the graphene surfaces of GO and GNP-based hybrids prepared by co-precipitation, as well as GNP/IO_{APTES} hybrid.

3.2. Raman spectroscopy of hybrids

Raman spectroscopy was used to determine the character of poly-aromatic carbon structures both of GNPs and GO precursors and their hybrids with deposited IO NPs. Fig. 4 shows the Raman spectra of the initial GO and GNPs as well as their hybrids GO/IO and GPN/IO. All spectra show three characteristic peaks for graphene structures [40,50], i.e. the D band at ~ 1340 cm^{-1} corresponding to the vibrations of sp^3-hybridized carbon atoms of the structural defects (such as vacancies, grain boundaries) and other disorders, and the G band at ~ 1580 cm^{-1} related to in-plane vibration of sp^2-bonded carbon atoms in a two-dimensional graphene hexagonal lattice with some sign of 2D peaks (2700 cm^{-1}). The intensity of the D band to G band (I_D/I_G) ratio is ~ 0.19 for GNPs and much higher, ~0.77, for the GO, which proves a significantly higher disorder degree of the GO than the GNPs structure.

After deposition of IO NPs onto GNPs and GO layers, the I_D/I_G ratios clearly increase for all hybrids, but differently depending on the hybrid preparation method. The most pronounced increase in the I_D/I_G ratio was observed for the GNP/IO_{cp} and GO/IO_{cp} hybrids. The smallest I_D/I_G ratios were noted for hybrids obtained by the deposition of IO_{APTES} NPs onto the GNPs and GO. This can be explained by the fact that IO_{APTES} NPs are attached largely at the edges of graphene layers, while the centers of the layers remain unchanged. The higher I_D/I_G ratios of hybrids compared to GNPs and GO precursors can be related to the higher disorder degree, larger number of defects, and smaller average size of sp^2 domains in the hybrid's structures. Increasing the disorder degree and number of defects in graphene sheets, and the formation of greater in number but smaller in size graphene areas, as a result of deposition of various metallic nanoparticles, have been previously reported [50,51].

The detailed Raman data, i.e., I_D/I_G values, Raman shift for D and G peaks, and the area ratio of D band to G band (A_D/A_G) are shown in Table 3. The I_D/I_G ratio determined at visible range of excitation laser energy can be used in the calculation of the crystallite sizes L_a of the graphene structures by Eq. (1) [52,53]:

$$L_a = \left(2.4 \cdot 10^{-10}\right)\lambda_l^4 \left(\frac{I_D}{I_G}\right)^{-1} \quad (1)$$

where λ_l is the Raman laser wavelength, and (2.4 10^{-10}) is the proportionality coefficient.

The L_a values calculated from Raman spectra variously correlate with electron microscopy observations and XRD measurements. Significant discrepancies in the average crystal size determined by Raman spectroscopy and XRD were observed for GNPs and GNP/IO_{APTES}, while values characterized for the graphite structure in the GO precursor were comparable. As an example, for hybrid materials, the average crystal size of the graphite domains in the GNP/IO_{cp} sample was about 45 nm, whereas the Raman scattering data gave 50 nm (Tables 2 and 3).

The characteristic peaks at lower wave numbers related to iron compounds deposited onto graphene surfaces illustrate that iron oxide particles are successfully anchored on the GO and GNP sheets.

The bands at 350–351 cm^{-1}, 481–486 cm^{-1}, and 686 cm^{-1} for the GO/IO hybrids observed in Fig. 4b, and the bands at 514 cm^{-1} and 667–681 cm^{-1} for the GNP/IO hybrids shown in Fig. 4d, can correspond to the A1g(1), E2g + E3g, A1g(2), and E5g modes of maghemite

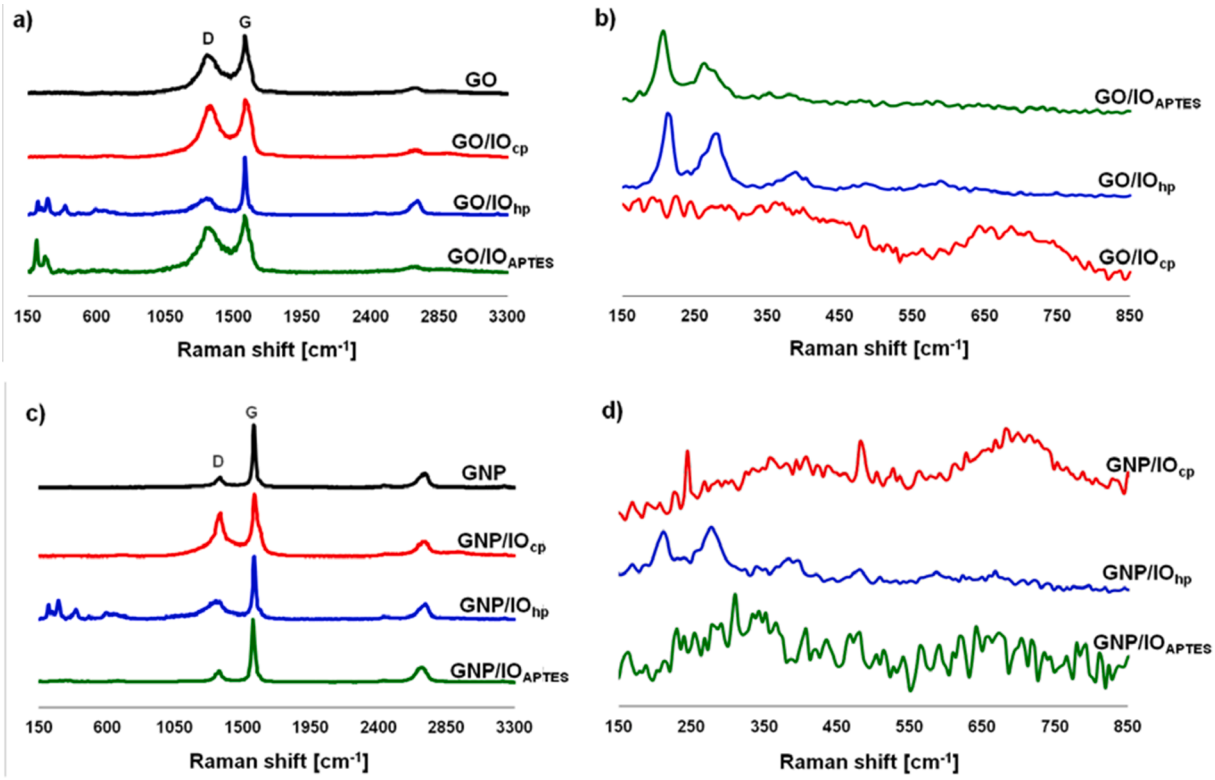

Fig. 4. Raman spectra for: a), b) the GO and GO/IO hybrids and c), d) pristine GNPs and GNP/IO hybrids. The spectra on the right side presents the narrow ranges spectrum with characteristic Raman peaks for iron compounds.

Table 3
Raman parameters of GNPs and GO precursors and their hybrids with IO NPs.

Sample	I_D/I_G	D (cm^{-1})	G (cm^{-1})	A_D/A_G	L_a [nm]
GO	0.765	1326	1578	1.996	25
GO/IO$_{cp}$	1.043	1337	1586	1.813	18
GO/IO$_{hp}$	0.847	1316	1571	3.889	23
GO/IO$_{APTES}$	0.836	1333	1574	2.262	23
GNPs	0.194	1349	1576	0.959	99
GNP/IO$_{cp}$	0.382	1352	1578	1.247	50
GNP/IO$_{hp}$	0.334	1330	1572	2.451	58
GNP/IO$_{APTES}$	0.232	1349	1571	1.022	83

(γ-Fe_2O_3) [54]. The bands of maghemite, in contrast to hematite and magnetite, are not well defined and are rather irregular and broad. The shape and intensity of these bands are related to the crystallinity degree of the maghemite phase. In the literature, the usual three broad bands around 350, 500 and 700 cm^{-1} related to maghemite but not present in the spectra of any other iron oxides or oxyhydroxides, are discussed [50,53,54]. Despite small differences in peak positions, the bands at approximately 243, 299, 385, and 479 cm^{-1} can be attributed to the oxyhydroxides (goethite, lepidocrocite and akaganeite). In spite of the similar chemical formula of the oxyhydroxides their Raman spectra show substantially distinct features, as described in the literature [50,55].

No magnetite NPs were identified as a separate iron phase from the XRD and Raman results of GO/IO$_{cp}$ and GNP/IO$_{cp}$ hybrids, but it has been referred to in other studies [14,25,36,56-59]. The presence of Fe_3O_4 NPs on the graphene surfaces were found for hybrids obtained by the co-precipitation method performed in nitrogen atmosphere.

3.3. XPS spectroscopy of hybrids

X-ray photoelectron spectroscopy was carried out to determine the surface and elemental compositions of graphene precursors and their hybrids with IO NPs. The XPS spectra of GO and GNPs and their hybrids with IO NPs are shown in Fig. 5.

The general XPS scans show that both GNP/IO and GO/IO hybrids mainly consist of C, O and Fe, which is consistent with the results of the EDX mapping. The characteristic peaks with various intensities around 285 eV and 533 eV can be clearly observed in all spectra and correspond to the C 1s and O 1s, respectively. Detailed data on the atomic concentration and C/O ratio of graphene materials before and after IO deposition processes are collected in Table 4.

The ratio of C/O is 2.98 for GO and 31.91 for GNPs, while the atomic concentration of the C element is 74.8 for GO and 96.6% for GNPs. The lowest C/O ratio for GO/IO$_{hp}$ indicates that iron compounds NPs can be most efficiently deposited onto GO surfaces. Higher C/O ratios for GO/IO$_{APTES}$ and GO/IO$_{cp}$ can indicate that the IO was deposited in a smaller amount on the graphene surface. A similar trend of changes in the iron content and C/O ratio was observed for the reduced form of graphene, GNPs.

The noticeable differences in the elemental compositions determined using the XPS technique compared to the values obtained by EDX are observed, and the XPS results are significantly lower in relation to the EDX data. However, contrary to EDX results, the iron element content determined by the XPS technique was higher for the hybrid prepared using GNPs as graphene support. The highest atomic concentration of Fe was found for hybrids prepared by homo-precipitation synthesis, i.e., 9.8% and 6.1% for GNP/IO$_{hp}$ and GO/IO$_{hp}$, respectively. These differences in atomic concentration between the XPS and EDX analysis can result from the different sample depths reached by the signal of these two techniques. In the EDX technique the signal comes from the depth of about 3 μm, while the XPS analysis mainly concerns the surface layer with the depth of 2–5 nm. The different depths of sample penetration in the case of the XPS and EDX techniques explains the different iron content in GO/IO and GNP/IO hybrids.

Fig. 6 presents high resolution XPS spectra for C 1s core-level (Fig. 6a

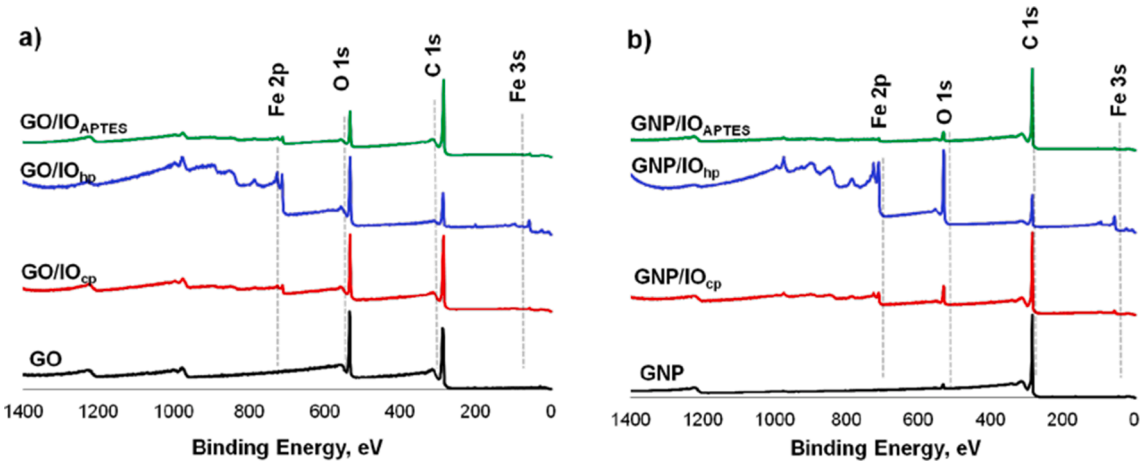

Fig. 5. XPS spectra with survey scan of a) GO precursor and GO-based hybrids with IO NPs, b) GNPs and GNP based hybrid materials with IO NPs.

Table 4
Atomic concentration and C/O ratio of graphene precursors and hybrids with IO NPs by XPS.

	C [at.%]	O [at.%]	Fe [at.%]	C/O
GO	74.8	25.1	–	2.98
GO/IO$_{cp}$	73.7	24.0	1.0	3.07
GO/IO$_{hp}$	47.7	42.9	6.1	1.13
GO/IO$_{APTES}$	80.7	17.3	1.0	4.67
GNPs	96.7	3.0	–	31.91
GNP/IO$_{cp}$	85.9	11.5	1.9	7.44
GNP/IO$_{hp}$	45.5	44.4	9.8	1.02
GNP/IO$_{APTES}$	91.1	6.3	0.7	14.51

and b), O 1s core-level (Fig. 6c and d), Fe 2p core-level (Fig. 6e and f), Fe 3s core-level (Fig. 6g and h) and valence bands (Fig. 6i and j). For GO and GO/IO hybrids, the C 1s XPS spectrum can be divided into three carbon component peaks with different binding energies at 284.6 eV, 286.8 eV and 289.2 eV that can be related to C—C/C═C bonds corresponding to the sp2-hybridized graphitic carbon in the basal plane, the C—O—C bonds, and the HO—C═O bonds, respectively [14,40,41]. The C 1s XPS spectra of GNPs and GNP/IO hybrids showed one pronounced peak at ~ 284.6 eV. Two additional peaks at 286 eV and 289 eV were found for the spectrum of GNP/IO$_{hp}$ corresponding to C—OH and C═O bonds, respectively.

The O1s spectra of GO precursor (Fig. 6c) showed two common peaks with binding energies of 532.6 eV corresponding to C═O bonds, and at 534.5 eV corresponding to C—O—C bonds. In the O 1s spectra of GO/IO$_{cp}$, GO/IO$_{hp}$ and GO/IO$_{APTES}$, peaks at 530 eV corresponding to Fe—O bonds were found.

Moreover, peaks at 531.8 eV corresponding to O—C═O groups for all GO/IO hybrids were identified. The peak at 532.8 eV related to C═O bonds was only observed for GO/IO$_{hp}$. The O 1s spectra of GNP and GNP based hybrids showed one peak at 531.4 eV corresponding to C═O bonds. The spectra of GNP/IO$_{cp}$, GNP/IO$_{hp}$ and GNP/IO$_{APTES}$ had a common peak at 530.2 eV corresponding to Fe-O resulting from the chemical bonding of the oxygen element (O^{2-} of Fe_2O_3), and GNP, GNP/IO$_{cp}$ and GNP/IO$_{APTES}$ have a peak at 533 eV corresponding to the C—OH bond. The XPS results indicate that GO and GNPs as graphene precursors, and Fe_2O_3 nanoparticles are combined well in the final hybrid structures. The separately deconvoluted O 1s peaks for GO, GNPs and their hybrids with IO NPs are presented in Supplementary Information (Fig. 1S). Fig. 6e and f show the high-resolution Fe 2p spectra of GO-based hybrids and GNP/IO hybrids, respectively. The presence of IO NPs on the surfaces of the hybrids was confirmed by typical XPS peaks for iron exhibited at the same binding energy, which proved a similar chemical state of iron. The spin-orbital coupling of Fe $2p_{3/2}$ and $Fe2p_{1/2}$ for both composites appeared at binding energies of ~ 712 and ~ 725 eV, which was consistent with data published elsewhere, and can be assigned to the Fe^{3+} of Fe_2O_3 [60,61]. A satellite peak in the middle at 719 eV was also observed.

Considering the deconvoluted O1s spectra of GO- and GNP-based hybrids with two peaks at 530.2 and 533–533.4 eV, indicating the presence of O^{2-} and OH— moieties, it could be stated that the iron particles exist in a mixed state of Fe_2O_3 and FeOOH.

In the case of the GNP/IO$_{APTES}$ sample, the Fe 2p iron line is only slightly visible in the survey spectrum (Fig. 5b). The high-resolution Fe 2p line was not observed, probably due to the low iron content deposited on the graphene surface. The atomic concentration determined for this sample showed an iron content of less than 1 at.% - approximately 0.7%. For this reason, no Fe 3 s line was observed.

Two-peak structures of Fe 3 s spectra were observed for hybrids obtained by the homo-precipitation route, reflecting a high-spin (94 eV) and a low-spin (100 eV) state. The Fe 3s line of GO/IO$_{APTES}$ exhibited one peak shifted at 102 eV. The additional peak on the Fe 3s spectra of GO/IO$_{cp}$ and GNP/IO$_{cp}$ hybrids was observed at binding energy ~ 88–89 eV. Generally, the peaks of the Fe 3s spectrum are weaker than the Fe 2p spectrum and are not usually used for quantification.

Analysis of the valence band region is another powerful tool to evaluate the π conjugated system [62]. Fig. 6i and 6j show high-resolution XPS spectra of the valence bands recorded for GO/IO and GNP/IO hybrids. Based on photoemission spectroscopic data for graphite, the region on GO and GNPs spectra from 2 to 12 eV above the Fermi level represented characteristics of C 2p electrons [62]. The spectra of GO/IO and GNP/IO hybrids consist of the main band with three-peak construction ~ 0–10 eV with a significantly higher intensity than for the GO and GNPs precursors. Moreover, the tetrahedral Fe^{3+} ions in γ -Fe_2O_3 gave a large intensity at lower energies and caused the increase of the main band at about 2.7 eV as Fe 3d derived states. The section 12–22 eV corresponds to the C 2s valence electrons, followed by the O 2s region at higher binding energy 22–32 eV. An oxygen-related peak O 2s of GNPs was shifted towards a lower binding energy in comparison to the O 2s peak observed for GO. The C 2s and O 2s bands for GNP/IO hybrids were shifted to higher binding energies in relation to the GNP O 2s peak [63].

3.4. Thermogravimetric analysis of hybrids

GO is a graphene form significantly less thermally stable than graphite and reduced graphene oxide due to the high concentration of oxygen groups on its surface. The C/O atomic ratio from XPS measurement of GO was 2.98 (Tab. 3). The initial mass loss up to 100 °C is

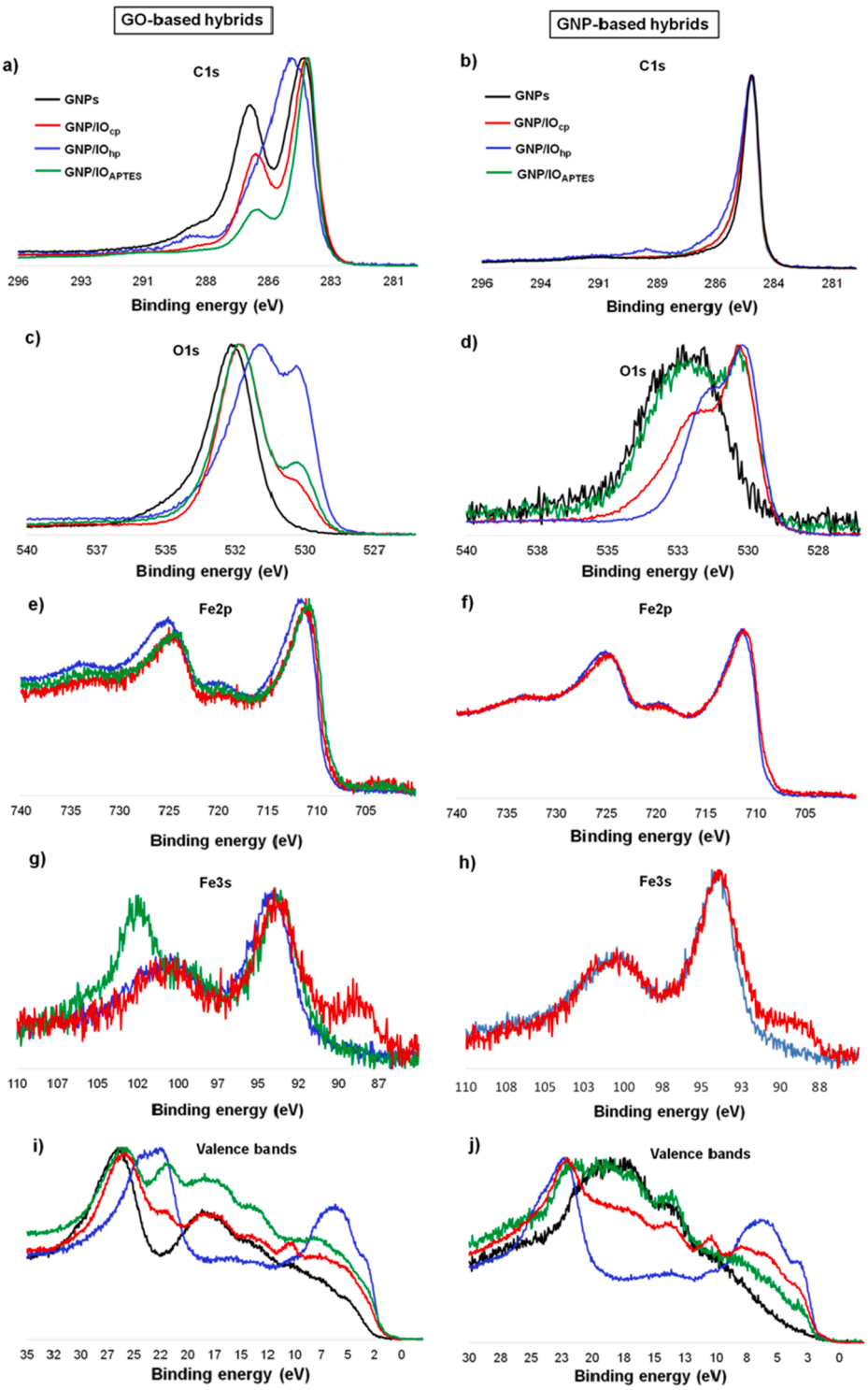

Fig. 6. High resolution XPS spectra of C 1s core-level (a, b), O1s core-level (c, d) Fe 2p core-level (e, f), Fe 3s (g, h), and spectra of valence bands region (i, j).

the effect of the release of water adsorbed on the hydrophilic GO surface (Fig. 7a), whereas at the temperature 220–280 °C, a significant mass loss results from the elimination of carboxyl and other oxygen functional groups. This step is followed by a slow continuous decay reaching a total mass loss of 32.4% at 1000 °C.

The GO/IO hybrids show a fall in the TG curves in the analogous temperature ranges, i.e., below 100 °C and 200–280 °C, however the mass losses at 200–300 °C for GO/IO$_{cp}$ (13.9%) and GO/IO$_{hp}$ (16.8%) were distinctly smaller as compared to GO (22.3%) and GO/IO$_{APTES}$ (21.9%). Most likely this was due to the protection of graphene surfaces by the deposited IO NPs. The mass loss for GO/IO$_{APTES}$ comparable to pure GO sample is probably the direct result of the attachment of IO NPs mainly at the edges of the graphene layers. The release of volatile products for the GO/IO$_{hp}$ sample takes place over a wider temperature range and a two-step process is observed. At the temperature between 500 °C and 760 °C, the sample GO/IO$_{hp}$ shows a slight mass loss. For other hybrids, a monotonic decrease on the TG curves above 500 °C is observed. These mass reductions in the hybrid materials can be attributed to the transformation of iron oxyhydroxide (FeOOH) to iron oxide Fe_2O_3 [64]. The occurrence of this chemical process was supported by

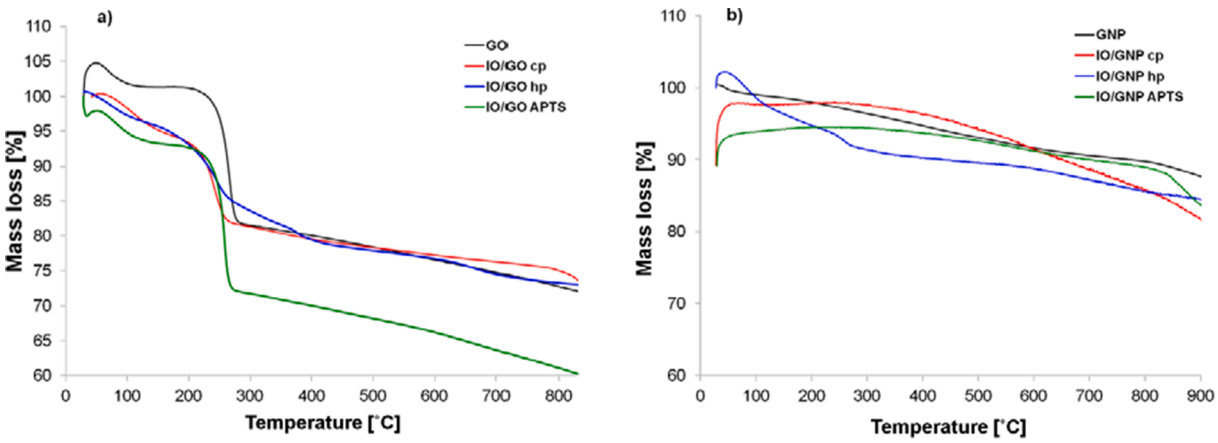

Fig. 7. TGA curves versus temperature for a) GO and GO/IO hybrids, b) GNPs and GNP/IO hybrids.

the thermal analyses of both maghemite and hematite particles [65]. The mass loss observed for silica coated iron oxide nanoparticles above 750 °C was explained as the effect of release of hydroxyl ions from these particles [66]. The mass loss in the TG curve at temperatures above 600 °C can be also assigned to the phase transformation of γ-Fe_2O_3 to α-Fe_2O_3. Özdemir et al. [67] studied the thermal stability of acicular maghemite by X-ray diffraction and magnetic measurements. They found that complete inversion of the γ- to α- Fe_2O_3 was not achieved even at 660 °C, and the final product was a two-phase mixture with 65% of the original, unchanged γ-Fe_2O_3. Additionally, the true Curie point of pure maghemite was found close to 645 °C. Tianshu et al [68], during a study of a nanostructured sample of γ-Fe_2O_3 doped with Y_2O_3, found the phase transition temperature of γ-Fe_2O_3 to α-Fe_2O_3 up to 725 °C. The authors noted the enhanced thermal stability of maghemite by doping it with other materials.

GNPs as expected, is more thermally stable than GO and has 11.5% mass reduction until 1000° C (Fig. 7b). The TG curves for GNP/IO hybrids show that their monotonic mass losses already start at around 500–600 °C, and at 1000 °C the loss is about 18.7% for GNP/IO_{APTES}, 19.4% for GNP/IO_{hp} and 26% for GNP/IO_{cp}.

3.5. Characteristics of GNP/IO_{cp} hybrids in nitrogen atmosphere

In this study the GO- and GNPs-IO hybrids obtained by co-precipitation method were found to contain iron (III) oxide nanoparticles in the form of maghemite embedded on the graphene sheets. Meanwhile, the literature reports on the synthesis of IO NPs using the co-precipitation method from analogous iron (III) and (II) salts show that the obtained IO NPs are in the form of magnetite (Fe_3O_4), or a mixture of magnetite and maghemite [14,20,25,44]. Therefore, it was decided to perform the co-precipitation procedure under nitrogen atmosphere to avoid the effect of oxygen on the reaction products and to obtain the hybrid of GNPs coated with magnetite nanoparticles (GNP/IO_{cpN}).

The SEM microphotograph of GNP/IO_{cpN} hybrid with unchanged sheet-like graphene structure evenly coated by IO NPs is shown in Fig. 8a. The concentration of IO NPs on the GNP sheets and their agglomeration tendency are definitely smaller than in the case of the hybrid obtained by co-precipitation in ambient atmosphere (see Fig. 1f). The EDX technique confirmed the lower relative atomic concentration of the Fe element and the C/O atomic ratio for the sample obtained under nitrogen, than the sample prepared in air atmosphere, equal to 2% and 5.1%, respectively. The TEM image (Fig. 8b) shows two-dimensional plates of iron oxide with a nearly spherical shape and a size of about 10–11 nm, definitely less agglomerated than in the GNP/IO_{cp} hybrid

The IO NPs deposited on the GNPs surfaces of GNP/IO_{cpN} hybrid were identified as the magnetite phase (Fe_3O_4) by XRD and Raman analyses. The XRD pattern (Fig. 9a) shows the peaks at 2θ values of around 26° and 43°assigned to diffraction of carbon planes of GNPs (space group $P6_3/mmc$, a = 2.46 Å, c = 6.71 Å ICDD; a = 2.46 Å, c = 6.72 Å calculated, crystallite size 40 nm, strain 0 %).). The peaks at 2θ values of around 30°, 35°, 58° and 62° can be indexed to Fe_3O_4 (ICDD #01–087-0244, space group Fd-3 m, a = 8.374 Å). The evaluated lattice parameters, average crystalline size, and strain are a = 8.396 Å, 10 nm, and 1.22, respectively, which confirms the presence of small crystallites.

Fig. 9b shows the Raman spectra of GNP/IO_{cpN} hybrid. The I_D/I_G of hybrid is ~ 0.225 proving the disorder degree of the graphene structure is higher compared to the initial GNPs as precursor, however lower than in the GNP/IO_{cp} hybrid obtained in ambient atmosphere. For Fe_3O_4 NPs the bands at 352, 486 and 672 cm^{-1} are observed despite a small signal-to-noise ratio.

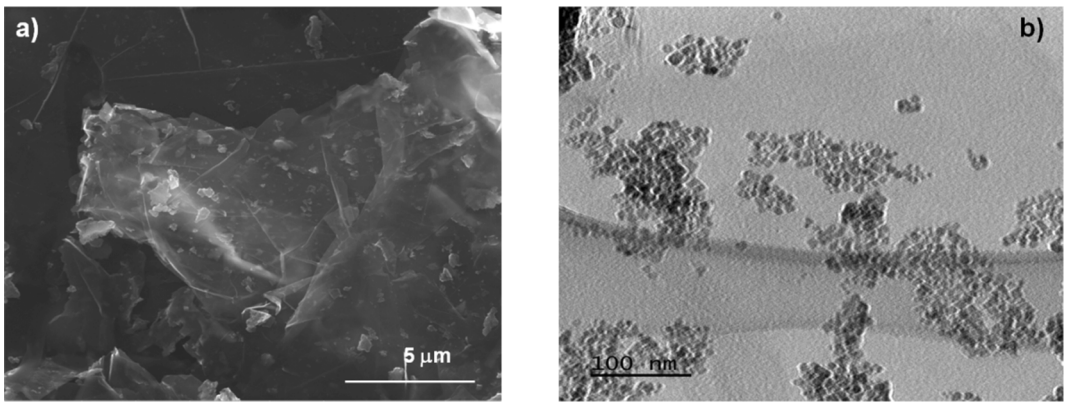

Fig. 8. SEM (a) and TEM (b) microphotographs of GNP/IO_{cpN} hybrid.

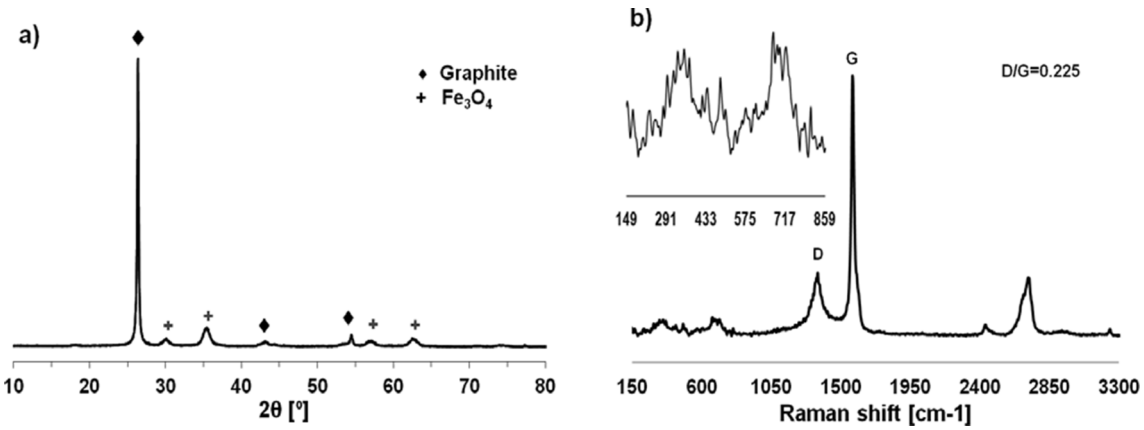

Fig. 9. X-Ray diffraction patterns (a) and Raman spectrum (b) of GNP/IO_{cpN} hybrid.

Based on the results presented above, it can be concluded that the co-precipitation procedure in inert atmosphere leads to a graphene-based hybrid material with evenly deposited magnetite nanoparticles only.

Summarizing, the results of our study of hybrid materials prepared by co-precipitation showed that iron oxides obtained in ambient atmosphere are inhomogeneous and different crystalline phases are deposited onto graphene sheets than those obtained in nitrogen atmosphere. The XRD data analyzed by Rietveld refinement revealed that in air atmosphere the main IO phase obtained is cubic structured γ-Fe_2O_3 (maghemite), whereas in nitrogen atmosphere the only IO phase obtained is Fe_3O_4 (magnetite). The vast majority of literature data regarding crystalline phases of IO NPs obtained using co-precipitation method reports that the magnetite phase is obtained both in ambient and nitrogen atmosphere. Only few mentions about the formation of the maghemite phase were found. Table 5 presents the comparison of the co-precipitation synthesis conditions and IO phases obtained, those found

Table 5
The comparison of the co-precipitation method conditions and final crystalline phase of IO NPs according to the literature data and the results of this study.

Method	Conditions	Crystalline phases	Size distribution	Source of the results
Ultrasonic-assisted chemical co-precipitation using high purity iron from iron ore tailings by an acidic leaching method	Fe^{3+} and Fe^{2+} molar ratio in $FeCl_3$ and $FeSO_4{\cdot}7H_2O$ solution was 1.5:1. Ultrasonic agitation NaOH Ambient atmosphere $C_{12}H_{25}OSO_3Na$ as surface active agent	Crystalline Fe_3O_4	Relatively narrow about15 nm	[69]
Chemical co-precipitation	$FeSO_4$ and $FeCl_3$ mixture The molar ratio of Fe^{2+}:Fe^{3+}=1:2 NaOH (pre-heated to 60 °C), ambient atmosphere	Crystalline Fe_3O_4	11.9 nm	[70]
Direct chemical co-precipitation	0.033 M $FeCl_2{\cdot}4H_2O$ and 0.066 M $FeCl_3{\cdot}6H_2O$ precursors solution with the pH 12 solution of Na_2CO_3	Poorly crystalline ferrihydrite phase and crystalline iron (II) hydroxide carbonate transformed into Fe_3O_4/γ-Fe_2O_3	about 4 nm	[71]
In situ chemical co-precipitation	0.106 mol $FeCl_2{\cdot}4H_2O$ and 0.212 mol $FeCl_3{\cdot}6H_2O$ in water and at 60 °C. Neutralization reaction with solution of 9 M NH_4OH Finally mixed at 500 rpm, for 90 min	γ-Fe_2O_3 only at the early stage Finally Fe_3O_4	9–15 nm	[72]
Chemical co-precipitation in presence of GO and chitozan	$FeCl_3{\cdot}6H_2O$ and $FeCl_2{\cdot}4H_2O$ in water (N_2 purification) Addition of 25% NH_4OH at 40 °C under N_2 gas with magnetic stirring the pH in the range 9–10.	Crystalline Fe_3O_4 on GO with chitosan	about 10 nm	[73]
Chemical co-precipitation	$FeCl_2{\cdot}4H_2O$ and $FeCl_3$ in distilled water with the mole ratio 1:2 throughout the experiment at 50 °C, pH 11.40 and 550 rpm	γ-Fe_2O_3	7–9 nm	[74]
Chemical co-precipitation in a continuous aqueous process using a micromixer system	Aqueous solution of ferric and ferrous sulphate with a molar ratio of 2:1 Fe(III) to Fe(II) 25% ammonium hydroxide to iron salts in volume ratio 1:19 Temperature 30 °C and 80 °C	γ-Fe_2O_3 + Fe_3O_4 (30 °C) γ-Fe_2O_3 (80 °C)	Agglomerates of 2 nm NPs Single NPs with dimensions of 7 nm	[75]
One-pot simplified chemical co-precipitation in the presence of MWCNTs	Aqueous solution of $FeCl_2{\cdot}4H_2O$ and $FeCl_3{\cdot}6H_2O$ with the mass ratio 1:2 Ammonium hydroxide until to pH 11–12	Fe_3O_4	12 nm	[76]
Chemical co-precipitation in the presence of GO and GNPs	Aqueous solution of $FeCl_2{\cdot}4H_2O$ and $FeCl_3{\cdot}6H_2O$ with the mass ratio 1:2 NH_4OH until to pH 11–12	γ-Fe_2O_3	Agglomerates of NPs:14 nm on the GO surface 8 nm on the GNPs	This work
Chemical co-precipitation in the presence of GNPs in nitrogen atmosphere	Aqueous solution of $FeCl_2{\cdot}4H_2O$ and $FeCl_3{\cdot}6H_2O$ with the mass ratio 1:2 8 mol of NaOH	Fe_3O_4	10 nm	This work

in the literature as well as from our research.

4. Conclusions

Hybrid graphene-inorganic materials were obtained by three methods: co-precipitation of iron (III) and (II) oxide from $FeCl_2$ and $FeCl_3$ solution onto graphene layers both in air and nitrogen atmosphere, homogeneous precipitation of Fe_2O_3 from $FeCl_3$ solution in the presence of graphene materials and grafting of Fe_2O_3 NPs functionalized with APTES on the graphene planes.

All methods mentioned, except the co-precipitation in nitrogen atmosphere, led to obtaining Fe_2O_3 NPs, while the latter one carried out with GNPs as graphene support led to obtaining Fe_3O_4 NPs.

SEM and TEM investigations showed that, depending on the preparation methods of the hybrids, various distributions and shapes of IO crystallites on the graphene layers were observed for GO and GNPs. The most homogeneous distribution, without agglomerates, was noted for hybrids obtained using the homo-precipitation method.

The XRD studies revealed that the maghemite (γ-Fe_2O_3) phase is dominant in all hybrid materials. Depending on the preparation method, various crystalline phases of iron (III) oxyhydroxide (FeOOH) as goethite, lepidocrocite, and akageneite were also observed. In the case of GNP-based hybrid prepared by co-precipitation procedure under nitrogen, the presence of magnetite phase Fe_3O_4 was confirmed in contrast to the maghemite γ-Fe_2O_3 occurring in GNP-based hybrid obtained in an air atmosphere.

XPS studies showed that in all hybrids, except GNP/IO_{cp} synthesized under nitrogen, iron is present mainly in the form of Fe^{3+}, which confirms the presence of phases detected by XRD.

The GNP/IO hybrids, in addition to being more thermally stable than GO-based ones, are easier to prepare as inexpensive, commercially available GNPs are used instead of Hummers-synthesized GO.

The wide spectrum of the obtained graphene/iron oxides hybrids is promising for the production of anisotropic polymer composites with increased thermal and electrical conductivity. These hybrids can also be the basis for further studies on preparation of more complex hybrid materials containing, in addition to IO NPs, other metal oxides as prospective magnetic fillers for production of EMI composite materials.

CRediT authorship contribution statement

Anastasiia Kobyliukh: Investigation, Methodology, Visualization. **Karolina Olszowska:** Investigation, Formal analysis, Visualization. **Marcin Godzierz:** Visualization, Investigation, Software. **Aleksandra Kordyka:** Formal analysis. **Jerzy Kubacki:** Investigation, Methodology. **Yevgen Mamunya:** Investigation, Writing – review & editing. **Sławomira Pusz:** Methodology, Writing – review & editing, Supervision. **Ivanka Stoycheva:** Investigation, Visualization. **Urszula Szeluga:** Conceptualization, Methodology, Writing – original draft.

Declaration of Competing Interest

The authors declare that they have no known competing financial interests or personal relationships that could have appeared to influence the work reported in this paper.

Acknowledgements

This work was partially realized in the frame of the project "Development of modern polymer nanocomposites with various graphene-like carbon nanofillers" between the Polish Academy of Sciences and the National Academy of Sciences of Ukraine (2018-2021).

Appendix A. Supplementary material

Supplementary data to this article can be found online at https://doi.org/10.1016/j.apsusc.2021.151567.

References

[1] J.H. Warner, F. Schaffel, A. Bachmatiuk, M.H. Rummeli, Graphene Fundamentals and Emergent Applications, 2013.
[2] J. Phiri, P. Gane, T.C. Maloney, General overview of graphene: Production, properties and application in polymer composites, Mater. Sci. Eng. B Solid-State Mater. Adv. Technol. 215 (2017) 9–28, https://doi.org/10.1016/j.mseb.2016.10.004.
[3] A.T. Smith, A.M. LaChance, S. Zeng, B. Liu, L. Sun, Synthesis, properties, and applications of graphene oxide/reduced graphene oxide and their nanocomposites, Nano, Mater. Sci. 1 (1) (2019) 31–47, https://doi.org/10.1016/j.nanoms.2019.02.004.
[4] T. Kuila, S. Bose, A.K. Mishra, P. Khanra, N.H. Kim, J.H. Lee, Chemical functionalization of graphene and its applications, Prog. Mater. Sci. 57 (7) (2012) 1061–1105, https://doi.org/10.1016/j.pmatsci.2012.03.002.
[5] U. Szeluga, S. Pusz, B. Kumanek, K. Olszowska, A. Kobyliukh, B. Trzebicka, Effect of graphene filler structure on electrical, thermal, mechanical, and fire retardant properties of epoxy-graphene nanocomposites - a review, Crit. Rev. Solid State Mater. Sci. (2019) 1–36, https://doi.org/10.1080/10408436.2019.1708702.
[6] A. Kazemi, N. Bahramifar, A. Heydari, S.I. Olsen, Synthesis and sustainable assessment of thiol-functionalization of magnetic graphene oxide and superparamagnetic Fe3O4@SiO2 for Hg(II) removal from aqueous solution and petrochemical wastewater, J. Taiwan Inst. Chem. Eng. 95 (2019) 78–93, https://doi.org/10.1016/j.jtice.2018.10.002.
[7] I. Huynen, S.H. Francisco Mederos-Henrya, Benoît.P. Pichonb, Y.T. Yaganga, A. Delcortec, C. Bailly, Decoration of nanocarbon solids with magnetite nanoparticles: towards microwave metamaterial absorbers, J. Mater. Chem. C. 4 (2016) 3290–3303, https://doi.org/10.1039/x0xx00000x.
[8] R. Atchudan, T.N. Jebakumar Immanuel Edison, S. Perumal, D. RanjithKumar, Y. R. Lee, Direct growth of iron oxide nanoparticles filled multi-walled carbon nanotube via chemical vapour deposition method as high-performance supercapacitors, Int. J. Hydrogen Energy. 44 (4) (2019) 2349–2360, https://doi.org/10.1016/j.ijhydene.2018.08.183.
[9] Z. Zhou, Q. Zhang, J. Sun, B. He, J. Guo, Q. Li, C. Li, L. Xie, Y. Yao, Metal-Organic Framework Derived Spindle-like Carbon Incorporated α-Fe_2O_3 Grown on Carbon Nanotube Fiber as Anodes for High-Performance Wearable Asymmetric Supercapacitors, ACS Nano 12 (2018) 3–4.
[10] Y. Luo, K. Wang, S. Luo, F. Zhao, H. Wu, K. Jiang, Q. Li, S. Fan, J. Wang, Three-Dimensional Carbon Nanotube/Transition-Metal Oxide Sponges as Composite Electrodes with Enhanced Electrochemical Performance, ACS Appl. Nano Mater. 1 (6) (2018) 2997–3005, https://doi.org/10.1021/acsanm.8b00606.
[11] Z. Cao, B. Wei, High rate capability of hydrogen annealed iron oxide-single walled carbon nanotube hybrid films for lithium-ion batteries, ACS Appl. Mater. Interfaces. 5 (20) (2013) 10246–10252, https://doi.org/10.1021/am403028z.
[12] J. Liu, M. Zheng, X. Shi, H. Zeng, H. Xia, Amorphous FeOOH Quantum Dots Assembled Mesoporous Film Anchored on Graphene Nanosheets with Superior Electrochemical Performance for Supercapacitors, Adv. Funct. Mater. 26 (6) (2016) 919–930, https://doi.org/10.1002/adfm.v26.610.1002/adfm.201504019.
[13] E.L. Albert, C.A. Che Abdullah, Y. Shiroshaki, Synthesis and characterization of graphene oxide functionalized with magnetic nanoparticle via simple emulsion method, Results Phys. 11 (2018) 944–950, https://doi.org/10.1016/j.rinp.2018.10.054.
[14] Y. Liu, M. Lu, K. Wu, S. Yao, X. Du, G. Chen, Q. Zhang, L. Liang, M. Lu, Anisotropic thermal conductivity and electromagnetic interference shielding of epoxy nanocomposites based on magnetic driving reduced graphene oxide@Fe_3O_4, Compos. Sci. Technol. 174 (2019) 1–10, https://doi.org/10.1016/j.compscitech.2019.02.005.
[15] X. Zhu, Y. Zhu, S. Murali, M.D. Stoller, R.S. Ruoff, Nanostructured reduced graphene oxide/Fe_2O_3 composite as a high-performance anode material for lithium ion batteries, ACS Nano 5 (4) (2011) 3333–3338, https://doi.org/10.1021/nn200493r.
[16] C. Song, W. Sun, Y. Xiao, X. Shi, Ultrasmall iron oxide nanoparticles: synthesis, surface modification, assembly, and biomedical applications, Drug Discov. Today. 24 (3) (2019) 835–844, https://doi.org/10.1016/j.drudis.2019.01.001.
[17] M.I. Khalil, Co-precipitation in aqueous solution synthesis of magnetite nanoparticles using iron(III) salts as precursors, Arab. J. Chem. 8 (2) (2015) 279–284, https://doi.org/10.1016/j.arabjc.2015.02.008.
[18] W. Wu, C.Z. Jiang, V.A.L. Roy, Designed synthesis and surface engineering strategies of magnetic iron oxide nanoparticles for biomedical applications, Nanoscale. 8 (2016) 19421–19474, https://doi.org/10.1039/c6nr07542h.
[19] M. Bashir, S. Riaz, S. Naseem, Effect of pH on Ferromagnetic Iron Oxide Nanoparticles, Elsevier Ltd. 2 (10) (2015) 5664–5668, https://doi.org/10.1016/j.matpr.2015.11.106.
[20] P. Wang, X. Wang, S. Yu, Y. Zou, J. Wang, Z. Chen, N.S. Alharbi, A. Alsaedi, T. Hayat, Y. Chen, X. Wang, Silica coated Fe3O4 magnetic nanospheres for high removal of organic pollutants from wastewater, Chem. Eng. J. 306 (2016) 280–288, https://doi.org/10.1016/j.cej.2016.07.068.
[21] C.S. Biju, Properties of α-Fe2O3/graphene nanohydrid synthesized by a simple hydrothermal/solution mixing method, Nano-Structures and Nano-Objects. 13 (2018) 44–50, https://doi.org/10.1016/j.nanoso.2017.12.005.
[22] T.A. Lastovina, A.P. Budnyk, M.A. Soldatov, Y.V. Rusalev, A.A. Guda, A.S. Bogdan, A.V. Soldatov, Microwave-assisted synthesis of magnetic iron oxide nanoparticles

in oleylamine–oleic acid solutions, Mendeleev Commun. 27 (5) (2017) 487–489, https://doi.org/10.1016/j.mencom.2017.09.019.
[23] K. Qiao, W. Tian, J. Bai, L. Wang, J. Zhao, Z. Du, X. Gong, Application of magnetic adsorbents based on iron oxide nanoparticles for oil spill remediation: A review, J. Taiwan Inst. Chem. Eng. 97 (2019) 227–236, https://doi.org/10.1016/j.jtice.2019.01.029.
[24] A. Ali, H. Zafar, I. Haq, A. Rehman Phull, J. Sarfraz, A. Hussain, Synthesis, characterization, applications, and challenges of iron oxide nanoparticles, Nanotechnol. Sci. Appl. 9 (2016) 49–67.
[25] H. Di, Z. Yu, Y. Ma, F. Li, L. Lv, Y. Pan, Y. Lin, Y. Liu, Y. He, Graphene oxide decorated with Fe3O4 nanoparticles with advanced anticorrosive properties of epoxy coatings, J. Taiwan Inst. Chem. Eng. 64 (2016) 244–251, https://doi.org/10.1016/j.jtice.2016.04.002.
[26] A.G. Magdalena, I.M.B. Silva, R.F.C. Marques, A.R.F. Pipi, P.N. Lisboa-Filho, M. Jafelicci, EDTA-functionalized Fe3O4 nanoparticles, J. Phys. Chem. Solids. 113 (2018) 5–10, https://doi.org/10.1016/j.jpcs.2017.10.002.
[27] S. Askari, H. Koolivand, M. Pourkhalil, R. Lotfi, A. Rashidi, Investigation of Fe_3O_4/Graphene nanohybrid heat transfer properties: Experimental approach, Int. Commun. Heat Mass Transf. 87 (2017) 30–39, https://doi.org/10.1016/j.icheatmasstransfer.2017.06.012.
[28] V. Chandra, J. Park, Y. Chun, J.W. Lee, I.-C. Hwang, K.S. Kim, Water-Dispersible Magnetite-Reduced Graphene Oxide Composites for Arsenic Removal, ACS Nano 4 (7) (2010) 3979–3986.
[29] L. Huang, F. Luo, Z. Chen, M. Megharaj, R. Naidu, Green synthesized conditions impacting on the reactivity of Fe NPs for the degradation of malachite green, Spectrochim. Acta - Part A Mol. Biomol. Spectrosc. 137 (2015) 154–159, https://doi.org/10.1016/j.saa.2014.08.116.
[30] M. Agharkar, S. Kochrekar, S. Hidouri, M.A. Azeez, Trends in green reduction of graphene oxides, issues and challenges: A review, Mater. Res. Bull. (2014), https://doi.org/10.1016/j.materresbull.2014.07.051.
[31] Z. Jiang, J. Li, H. Aslan, Q. Li, Y. Li, M. Chen, Y. Huang, J.P. Froning, M. Otyepka, R. Zbořil, F. Besenbacher, M. Dong, A high efficiency H2S gas sensor material: Paper like Fe_2O_3/graphene nanosheets and structural alignment dependency of device efficiency, J. Mater. Chem. A. 2 (2014) 6714–6717, https://doi.org/10.1039/c3ta15180h.
[32] V.N. Palakollu, T.E. Chiwunze, C. Liu, R. Karpoormath, Electrochemical sensitive determination of acetaminophen in pharmaceutical formulations at iron oxide/graphene composite modified electrode, Arab. J. Chem. (2019) 1–8, https://doi.org/10.1016/j.arabjc.2019.08.001.
[33] S. Maji, A. Ghosh, K. Gupta, A. Ghosh, U. Ghorai, A. Santra, P. Sasikumar, U. C. Ghosh, Efficiency evaluation of arsenic(III) adsorption of novel graphene oxide@iron-aluminium oxide composite for the contaminated water purification, Sep. Purif. Technol. 197 (2018) 388–400, https://doi.org/10.1016/j.seppur.2018.01.021.
[34] P. Huang, W. Tao, H. Wu, X. Li, T. Yin, Q. Zhang, W. Qi, G. Gao, D. Cui, N-doped coaxial CNTs@A-Fe_2O_3@C nanofibers as anode material for high performance lithium ion battery, J. Energy Chem. 27 (5) (2018) 1453–1460, https://doi.org/10.1016/j.jechem.2017.09.011.
[35] W. Sheng, Q. Xu, J. Chen, H. Wang, Z. Ying, R. Gao, X. Zheng, X. Zhao, Electrochemical sensing of hydrogen peroxide using nitrogen-doped graphene/porous iron oxide nanorod composite, Mater. Lett. 235 (2019) 137–140, https://doi.org/10.1016/j.matlet.2018.10.022.
[36] C. Guan, J. Liu, Y. Wang, L. Mao, Z. Fan, Z. Shen, H. Zhang, J. Wang, Iron Oxide-Decorated Carbon for Supercapacitor Anodes with Ultrahigh Energy Density and Outstanding Cycling Stability, ACS Nano 9 (5) (2015) 5198–5207.
[37] M. Nisar, C.P. Bergmann, J. Geshev, R. Quijada, G.B. Galland, Synthesis and characterization of polypropylene/iron encapsulated carbon nanotube composites with high magnetic response at room temperature, Polymer (Guildf). 118 (2017) 68–74, https://doi.org/10.1016/j.polymer.2017.04.067.
[38] Y. Kang, X. Yu, M. Kota, H.S. Park, Carbon nanotubes branched on three-dimensional, nitrogen-incorporated reduced graphene oxide/iron oxide hybrid architectures for lithium ion battery anode, J. Alloys Compd. 726 (2017) 88–94, https://doi.org/10.1016/j.jallcom.2017.07.264.
[39] S.-H. Lee, V. Sridhar, J.-H. Jung, K. Karthikeyan, Y.-S. Lee, R. Mukherjee, N. Koratkar, I.-K. Oh, Graphene-nanotube-iron hierarchical nanostructure as lithium ion battery anode, ACS Nano 7 (5) (2013) 4242–4251, https://doi.org/10.1021/nn4007253.
[40] B. Kumanek, U. Szeluga, S. Pusz, A.F. Borowski, P.S. Wrobel, A. Bachmatiuk, J. Kubacki, M. Musioł, O. Maruzhenko, B. Trzebicka, Multi-layered graphenic structures as the effect of chemical modification of thermally treated anthracite, Fullerenes Nanotub. Carbon Nanostructures. 26 (7) (2018) 405–416, https://doi.org/10.1080/1536383X.2018.1441827.
[41] H.M. Rietveld, Line profiles of neutron powder-diffraction peaks for structure refinement, Acta Crystallogr. 22 (1967) 151–152, https://doi.org/10.1107/s0365110x67000234.
[42] H.M. Rietveld, A profile refinement method for nuclear and magnetic structures, J. Appl. Crystallogr. 2 (1969) 65–71, https://doi.org/10.1107/s0021889869006558.
[43] M. Karolus, E. Łągiewka, Crystallite size and lattice strain in nanocrystalline Ni-Mo alloys studied by Rietveld refinement, J. Alloys Compd. 367 (1-2) (2004) 235–238, https://doi.org/10.1016/j.jallcom.2003.08.044.
[44] H. Kalil, S. Maher, T. Bose, M. Bayachou, Manganese Oxide/Hemin-Functionalized Graphene as a Platform for Peroxynitrite Sensing, J. Electrochem. Soc. 165 (12) (2018) G3133–G3140, https://doi.org/10.1149/2.0221812jes.
[45] J. Li, D. Li, S. Zhang, H. Cui, C. Wang, Analysis of the factors affecting the magnetic characteristics of nano-Fe3O4 particles, Chinese Sci. Bull. 56 (8) (2011) 803–810, https://doi.org/10.1007/s11434-010-4126-z.
[46] L. Kou, C. Gao, Making silica nanoparticle-covered graphene oxide nanohybrids as general building blocks for large-area superhydrophilic coatings, Nanoscale 3 (2) (2011) 519–528, https://doi.org/10.1039/C0NR00609B.
[47] P. Ayyub, M. Multani, M. Barma, V.R. Palkar, R. Vijayaraghavan, Size-induced structural phase transitions and hyperfine properties of microcrystalline Fe_2O_3, J. Phys. C Solid State Phys. 21 (11) (1988) 2229–2245, https://doi.org/10.1088/0022-3719/21/11/014.
[48] E. Malicka, M. Karolus, J. Panek, Z. Stokłosa, T. Groń, A. Gudwański, B. Sawicki, J. Goraus, Effect of crystallite size on electrical and magnetic properties of $CuCr_2S_4$ nanoparticles obtained by mechanical alloying from sulphides, Phys. B Condens. Matter. 581 (2020), https://doi.org/10.1016/j.physb.2019.411829.
[49] E. Malicka, M. Karolus, T. Groń, A. Gudwański, A. Ślebarski, J. Goraus, M. Oboz, B. Sawicki, J. Panek, Influence of crystallite size on the magnetic order in semiconducting ZnCr2Se4 nanoparticles, Materials (Basel). 12 (2019) 1–10, https://doi.org/10.3390/ma122333947.
[50] Q. Yang, R. Bi, K.-chuen. Yung, M. Pecht, Electrochemically reduced graphene oxides/nanostructured iron oxides as binder-free electrodes for supercapacitors, Electrochim. Acta. 231 (2017) 125–134, https://doi.org/10.1016/j.electacta.2017.02.045.
[51] Z. Ji, X. Shen, M. Li, H. Zhou, G. Zhu, K. Chen, Synthesis of reduced graphene oxide/CeO2 nanocomposites and their photocatalytic properties, Nanotechnology. 24 (2013), https://doi.org/10.1088/0957-4484/24/11/115603.
[52] L.G. Caṇado, K. Takai, T. Enoki, M. Endo, Y.A. Kim, H. Mizusaki, A. Jorio, L. N. Coelho, R. Magalhães-Paniago, M.A. Pimenta, General equation for the determination of the crystallite size la of nanographite by Raman spectroscopy, Appl. Phys. Lett. 88 (2006) 1–4, https://doi.org/10.1063/1.2196057.
[53] I.S. Lyubutin, A.O. Baskakov, S.S. Starchikov, K.Y. Shih, C.R. Lin, Y.T. Tseng, S. S. Yang, Z.Y. Han, Y.L. Ogarkova, V.I. Nikolaichik, A.S. Avilov, Synthesis and characterization of graphene modified by iron oxide nanoparticles, Mater. Chem. Phys. 219 (2018) 411–420, https://doi.org/10.1016/j.matchemphys.2018.08.042.
[54] H. Zhang, Q. Gao, K. Yang, Y. Tan, W. Tian, L. Zhu, Z. Li, C. Yang, Solvothermally induced α-Fe2O3/graphene nanocomposites with ultrahigh capacitance and excellent rate capability for supercapacitors, J. Mater. Chem. A. 3 (44) (2015) 22005–22011, https://doi.org/10.1039/C5TA06668A.
[55] C.W. Brown, R.J. Thibeau, R.H. Heidersbach, Raman Spectra of Possible Corrosion Products of Iron, Appl. Spectrosc. Vol. 32, Issue 6, Pp. 532-535. 32 (1978) 532–535. https://www.osapublishing.org/as/abstract.cfm?URI=as-32-6-532 (accessed May 12, 2021).
[56] S. Vadahanambi, S.-H. Lee, W.-J. Kim, I.-K. Oh, Arsenic Removal from Contaminated Water Using Three-Dimensional Graphene-Carbon Nanotube-Iron Oxide Nanostructures, Environ. Sci. Technol. 47 (2013), https://doi.org/10.1021/es401389g, 130904083814004.
[57] S.H. Lee, D. Kang, I.K. Oh, Multilayered graphene-carbon nanotube-iron oxide three-dimensional heterostructure for flexible electromagnetic interference shielding film, Carbon N. Y. 111 (2017) 248–257, https://doi.org/10.1016/j.carbon.2016.10.003.
[58] W. Chen, X. Yang, J. Huang, Y. Zhu, Y. Zhou, Y. Yao, C. Li, Iron oxide containing graphene/carbon nanotube based carbon aerogel as an efficient E-Fenton cathode for the degradation of methyl blue, Electrochim. Acta. 200 (2016) 75–83, https://doi.org/10.1016/j.electacta.2016.03.044.
[59] V.N. Palakollu, T.E. Chiwunze, C. Liu, R. Karpoormath, Electrochemical sensitive determination of acetaminophen in pharmaceutical formulations at iron oxide/graphene composite modified electrode, Arab. J. Chem. 13 (2) (2020) 4350–4357, https://doi.org/10.1016/j.arabjc.2019.08.001.
[60] G.S. Parkinson, Iron oxide surfaces, Surf. Sci. Rep. 71 (1) (2016) 272–365, https://doi.org/10.1016/j.surfrep.2016.02.001.
[61] C. de Alwis, T.R. Leftwich, P. Mukherjee, A. Denofre, K.A. Perrine, Spontaneous selective deposition of iron oxide nanoparticles on graphite as model catalysts, Nanoscale Adv. 1 (12) (2019) 4729–4744, https://doi.org/10.1039/C9NA00472F.
[62] H. Shin, K.K. Kim, A. Benayad, S. Yoon, H.K. Park, I. Jung, M.H. Jin, H. Jeong, J. M. Kim, J. Choi, Y.H. Lee, Efficient reduction of graphite oxide by sodium borohydride and its effect on electrical conductance, Adv. Funct. Mater. 19 (12) (2009) 1987–1992, https://doi.org/10.1002/adfm.v19:1210.1002/adfm.200900167.
[63] T. Fujii, F.M.F. de Groot, G.A. Sawatzky, F.C. Voogt, T. Hibma, K. Okada, In situ xps analysis of various iron oxide films grown by (formula presented)-assisted molecular-beam epitaxy, Phys. Rev. B - Condens. Matter Mater. Phys. 59 (1999) 3195–3202, https://doi.org/10.1103/PhysRevB.59.3195.
[64] R. Zboril, M. Mashlan, D. Petridis, Iron (III) Oxides from Thermal Processes s Synthesis, Chem. Mater. 14 (2002) 969–982.
[65] O.N. Shebanova, P. Lazor, Raman study of magnetite (Fe3O4): Laser-induced thermal effects and oxidation, J. Raman Spectrosc. 34 (2003) 845–852, https://doi.org/10.1002/jrs.1056.
[66] Y.-S. Li, J.S. Church, A.L. Woodhead, F. Moussa, Preparation and characterization of silica coated iron oxide magnetic nano-particles, Spectrochim. Acta - Part A Mol, Biomol. Spectrosc. 76 (5) (2010) 484–489, https://doi.org/10.1016/j.saa.2010.04.004.
[67] O. Ozdemir, S.K. Banerjee, reflections inversion. The, Geophys. Res. Lett. 11 (1984) 161–164.
[68] Z. Tianshu, L. Hongmei, Z. Huanxing, Z. Ruifang, S. Yusheng, Synthesis and gas-sensing characteristics of high thermostability γ-Fe_2O_3 powder, Sensors Actuators, B Chem. 32 (1996) 181–184, https://doi.org/10.1016/S0925-4005(97)80026-3.

[69] S. Wu, A. Sun, F. Zhai, J. Wang, W. Xu, Q. Zhang, A.A. Volinsky, Fe_3O_4 magnetic nanoparticles synthesis from tailings by ultrasonic chemical co-precipitation, Mater. Lett. 65 (12) (2011) 1882–1884, https://doi.org/10.1016/j.matlet.2011.03.065.
[70] X. Xie, X. Zhang, J. Chen, X. Tang, M. Wang, L. Zhang, Z. Guo, W. Shen, Fe_3O_4-solamargine induces apoptosis and inhibits metastasis of pancreatic cancer cells, Int. J. Oncol. 54 (2019) 905–915, https://doi.org/10.3892/ijo.2018.4637.
[71] A.P. LaGrow, M.O. Besenhard, A. Hodzic, A. Sergides, L.K. Bogart, A. Gavriilidis, N. T.K. Thanh, Unravelling the growth mechanism of the co-precipitation of iron oxide nanoparticles with the aid of synchrotron X-Ray diffraction in solution, Nanoscale. 11 (14) (2019) 6620–6628, https://doi.org/10.1039/C9NR00531E.
[72] H. Rashid, M.A. Mansoor, B. Haider, R. Nasir, S.B. Abd Hamid, A. Abdulrahman, Synthesis and characterization of magnetite nano particles with high selectivity using in-situ precipitation method, Sep. Sci. Technol. 55 (6) (2020) 1207–1215, https://doi.org/10.1080/01496395.2019.1585876.
[73] N. Ye, Y. Xie, P. Shi, T. Gao, J. Ma, Synthesis of magnetite/graphene oxide/chitosan composite and its application for protein adsorption, Mater. Sci. Eng. C. 45 (2014) 8–14, https://doi.org/10.1016/j.msec.2014.08.064.
[74] B.H. Hui, M.N. Salimi, Production of Iron Oxide Nanoparticles by Co-Precipitation method with Optimization Studies of Processing Temperature, pH and Stirring Rate, IOP Conf. Ser. Mater. Sci. Eng. 743 (2020), https://doi.org/10.1088/1757-899X/743/1/012036.
[75] M. Girod, S. Vogel, W. Szczerba, A.F. Thünemann, How temperature determines formation of maghemite nanoparticles, J. Magn. Magn. Mater. 380 (2015) 163–167, https://doi.org/10.1016/j.jmmm.2014.09.057.
[76] H. Zhang, G. Zhang, J. Li, X. Fan, Z. Jing, J. Li, X. Shi, Lightweight, multifunctional microcellular PMMA/Fe_3O_4@MWCNTs nanocomposite foams with efficient electromagnetic interference shielding, Compos. Part A Appl. Sci. Manuf. 100 (2017) 128–138, https://doi.org/10.1016/j.compositesa.2017.05.009.